



TECHNISCHE
UNIVERSITÄT
WIEN
Vienna | Austria

Diploma Thesis

Formation of wear resistant tribofilms in sliding contacts by using Si-based organic precursors

carried out at the

Institute of Engineering Design and Product Development

at TU WIEN

under the supervision of **Univ. Prof. Dipl.-Ing. Dr.-Ing. Carsten Gachot**

by

Tobias Tassilo Trubrig

Vienna, April 2019

Signature

Abstract

Tribofilms play a major role in minimizing friction and wear of lubricated contacts and can be generated in a tribological system due to different mechanochemical interactions between the lubricant and the surface of the friction partners.

The aim of this work was to test 3 organosilicon compounds, i.e. bis(trimethylsilyl)carbodiimide, poly(methylphenylsiloxane) and trimethoxyphenylsilane, for their behaviour in friction contacts at different temperatures on classical rolling bearing steel (100Cr6) and to determine their potential for hot forming processes in metal processing. The tests were carried out on an oscillating friction wear test rig SRV (ball/disc). Apart from the determination of friction coefficient and wear volume, the surface of the formed wear tracks was analyzed by scanning electron microscopy, Raman spectroscopy, transmission electron microscopy and X-ray photoelectron spectroscopy in order to understand the interactions of the 3 precursors with the steel and to characterize the formed tribolayers.

With regard to friction behaviour and tribofilm formation, it was shown that trimethoxyphenylsilane in particular has a promising potential in terms of hot forming processes, With regard to the friction behaviour and tribofilm formation it could be shown that trimethoxyphenylsilane in particular has a promising potential with regard to hot forming processes, since the friction did not increase strongly with increasing temperature or even partly decreased and a tribofilm could be detected.

Kurzfassung

Tribofilme spielen eine große Rolle in der Reibungs- und Verschleißminimierung geschmierter Kontakte und können in einem tribologischen System durch unterschiedliche mechanochemische Wechselwirkungen zwischen dem Schmierstoff und der Oberfläche der Reibungspartner entstehen.

Ziel dieser Arbeit war es 3 siliziumorganische Verbindungen, i.e. Bis(trimethylsilyl)carbodiimid, Poly(methylphenylsiloxan) und Trimethoxyphenylsilan, auf deren Verhalten im Reibungskontakt bei unterschiedlichen Temperaturen auf klassischem Wälzlagerstahl (100Cr6) zu testen und deren Potential für Warmumformungsprozesse in der Metallverarbeitung zu ermitteln. Die Versuche wurden an einem Schwing-Reibverschleiß-Prüfstand SRV (Kugel/Scheibe) durchgeführt. Abgesehen von der Ermittlung von Reibungskoeffizient und Verschleißvolumen wurde die Oberfläche der gebildeten Verschleißspuren mit Hilfe von Rasterelektronenmikroskopie, Ramanspektroskopie, Transmissionselektronenmikroskopie und Röntgenphotoelektronenspektroskopie analysiert um die Wechselwirkungen der 3 Präkursoren mit dem Stahl nachvollziehen zu können und die gebildeten Triboschichten charakterisieren zu können.

In Bezug auf Reibungsverhalten und Tribofilmbildung zeigte sich, dass besonders Trimethoxyphenylsilan ein vielversprechendes Potential in Hinblick auf Warmumformprozesse besitzt, da die Reibung mit steigender Temperatur nicht stark anstieg beziehungsweise teilweise sogar sank und ein Tribofilm nachgewiesen werden konnte.

Acknowledgement

I would like to dedicate this work to all those who made it possible and supported me.

First of all I would like to thank **Univ.Prof. Dipl.-Ing. Dr.-Ing. Carsten Gachot** for giving me the opportunity to write my thesis under his supervision. He took a lot of time to present his research to me and suggest potential topics for my thesis. Also during the execution of my thesis he encouraged me often and gave me recommendations and advice. It is also thanks to him that I was able to exchange ideas about my research topic with professors and students during a short stay at the LTU in Luleå and to make further experiments.

Special thanks I want to send to **Dr. Manel Rodriguez Ripoll**, who was involved in the topic development and supported me in my practical work at AC2T in Wiener Neustadt. If I had any questions, I could always come to him and he made some very helpful and interesting suggestions for carrying out my experiments.

As already mentioned I had the opportunity to spend a week in Luleå in the course of my diploma thesis. **Professor Ichiro Minami** was my contact person and supervised my experiments there. He gave me some valuable tips and always was available when I needed him. I really appreciated his friendly and helpful nature. He was also involved in the topic development of my diploma thesis.

In addition, I would like to thank everyone who helped me with my different analysis methods. On the one hand I would like to thank **Dr. Johannes Bernardi** and his team for all measurements at the USTEM, on the other hand I would like to thank **Dr. Annette Foelske-Schmitz** and **Dr. Markus Sauer** from AIC for the XPS measurements. Thanks also to **Dr. Bernhard Kohlhauser**, who helped me with the Raman analyses.

Last but definitely not least I would like to thank my family and friends for their support. They kept my head up and I cannot imagine how the last months would have been without them.

This work was funded by the Austrian COMET-Program (Project K2 X Tribology, Grant No. 849109) and has been carried out within the Excellence Centre of Tribology.

Affidavit

I declare in lieu of oath, that I wrote this thesis and performed the associated research myself, using only the literature cited in this volume. If text passages from sources are used literally, they are marked as such.

I confirm that this work is original and has not been submitted elsewhere for any examination, nor is it currently under consideration for a thesis elsewhere.

I confirm that going to press of this thesis needs confirmation of the examination committee.

Signature: _____

Vienna, April 2019

Content

1 INTRODUCTION	1
2 THEORETICAL BACKGROUND.....	2
2.1 Friction.....	2
2.1.1 Coefficient of friction.....	2
2.1.2 Tribological system.....	3
2.1.3 Friction conditions.....	4
2.1.4 Types of friction.....	6
2.2 Wear.....	7
2.2.1 Wear mechanisms.....	7
2.2.2 Wear parameters.....	10
2.3 Friction modification	11
2.3.1 Dissipation of friction energy	11
2.3.2 Anticipating friction.....	13
2.3.3 Tribofilms.....	14
2.4 Chemistry of the precursors.....	16
2.4.1 Bis(trimethylsilyl)carbodiimide (precursor 1).....	17
2.4.2 Poly(methylphenyl)siloxane (precursor 2)	18
2.4.3 Trimethoxyphenylsilane (precursor 3)	18
3 METHODOLOGY	19
3.1 Tribometer	19
3.2 Confocal microscopy	20
3.3 Scanning electron microscopy and energy-dispersive X-ray spectroscopy	20
3.3.1 Scanning electron microscopy.....	20
3.3.2 Energy-dispersive X-ray spectrometry	22
3.4 Raman spectroscopy	23
3.5 Focused ion beam.....	24
3.5.1 Preparation of a TEM-foil	25
3.6 Transmission electron microscopy.....	25
3.7 X-ray photoelectron spectroscopy	26
3.8 Viscometer	28

4 RESULTS & DISCUSSION	29
4.1 No precursor	31
4.1.1 Friction analysis	31
4.1.2 Wear	32
4.1.3 SEM & EDS analysis	32
4.2 Precursor 1	34
4.2.1 Friction analysis	34
4.2.2 Wear	34
4.2.3 SEM & EDS analysis	35
4.2.4 Raman analysis	37
4.2.5 TEM analysis	38
4.3 Precursor 2	40
4.3.1 Friction analysis	40
4.3.2 Wear	40
4.3.3 SEM & EDS analysis	41
4.3.4 Raman analysis	42
4.4 Precursor 3	45
4.4.1 Friction analysis	45
4.4.2 Wear	47
4.4.3 SEM & EDS analysis	48
4.4.4 Raman analysis	49
4.4.5 TEM analysis	50
4.5. Comparison.....	52
4.5.1 Friction analysis	52
4.5.2 Wear	53
4.5.3 SEM analysis	54
4.5.4 XPS analysis	55
5 CONCLUSION	60
6 OUTLOOK.....	61
NOMENCLATURE.....	62
REFERENCES.....	64
LIST OF FIGURES	71
LIST OF TABLES.....	74

1 Introduction

Friction is a phenomenon we encounter every day. Sometimes the importance of friction is obvious, for example when you have to decelerate a vehicle abruptly and unexpectedly. However, in the use of contact lenses, most people probably would not immediately assign a fundamental role to friction. These two examples show that friction can be considered positive in the life-saving role on the one hand, but can also often be evaluated negatively in the case of the contact lenses on the other hand. It is therefore quite reasonable that there is great interest in influencing and anticipating friction in given processes and applications.

The automobile is a good example to underline the significance of friction in numerical terms and shows that this science field can play a big role in energy saving. Only 21.5 % of the energy consumed is actually used to move the vehicle. Friction losses are responsible for one-third of the total energy loss of fuel energy [1].

Apart from energy savings or energy losses, friction can also have a big impact on the course of chemical reactions. This interaction of friction and chemistry is designated by the term tribochemistry. Lighters or matches are prime examples since the fire is generated by friction. With its help it is possible to lower the temperature at which chemical reactions start by several hundred degrees and thus observing high temperature effects already at colder temperatures [2].

One possible way of benefiting from this reaction-enhancing effect is the use of additives in lubricants that can be activated by friction and react with the contact surfaces [3]. The tribolayers formed in this way can possibly have a friction and wear-reducing effect [4] on the basic bodies and therefore play an increasingly important role in tribology.

It has been reported that some organosilica networks show a friction-reducing effect in experiments at elevated temperatures [5]. It is also known that it is possible to obtain ceramic materials from organosilicon polymers under the influence of high temperatures (keyword Polymer Derived Ceramics PDCs) [6]. This class of chemical compounds therefore represents an interesting option for potential additives for wear protection in the hot forming of metals. The aim of this work is to increase the knowledge of their possible use in this field.

2 Theoretical background

2.1 Friction

Friction is a mechanical force, that can either resist (kinetic or dynamic friction) or hinder (static friction) the movement between touching surfaces. The difference lies in the relative motion. Together it is called external friction and is especially caused by microscopic contacts between two sliding surfaces. Apart from external friction there is also internal friction, which is better known under the name viscosity and is part of rheology [7].

2.1.1 Coefficient of friction

An important value in terms of friction and in particular in this thesis is the coefficient of friction (COF). It is defined as the dimensionless ratio between the friction force F and the normal force N . Usually symbolized by the letter μ or f it is not a material, but a system property. This scalar value has to be determined by empirical measurements and ranges between near zero and greater than one. It is common to differentiate between the kinetic/dynamic and the static coefficient of friction, where they refer to conditions of macroscopic relative motion of two bodies and the maximum force that must be overcome to initiate macroscopic motion between two bodies, respectively [7].

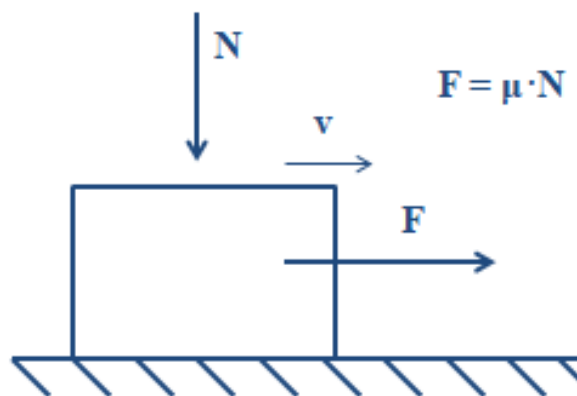


Figure 1: Coefficient of friction adapted from [7]

Figure 1 shows the definition of the COF. Basically, this definition is nothing other than the law of friction according to *Guillaume Amontons* [8]. It states that the friction force in solid friction is proportional to the normal force and that the proportionality factor is called the coefficient of friction. In addition, the friction force is independent of the nominal geometric contact area, but dependent on the real area of contact.

2.1.2 Tribological system

Friction and wear are not material properties and can therefore not be characterized by material characteristics. They are system properties and it is necessary to analyze and consider the various parameters and influencing variables of the tribological system concerned. These systems can be categorized according to their functional task. They can convert mechanical energy, information, or materials. The system structures required for the function always have 4 system elements: a base body, a counter body, an intermediate medium and the environment. The base and counter-body are the active surfaces which are exposed to tribological stresses. Friction and wear are caused by dissipation effects in locally and temporally stochastically distributed micro-contacts depending on the stress collective and the system structure. Since a tribological system describes only a part of a system and it is necessary to describe the entire system, a distinction is made between open and closed tribological systems [7, 9].

- Open tribological systems have the feature that one or more tribo elements are not in permanent tribological contact and are moved through the system [7].
- In closed tribological systems however the system elements are permanent parts over the duration of loading and constantly attend the tribological processes [7].

Figure 2 shows a schematic illustration of a tribological system.

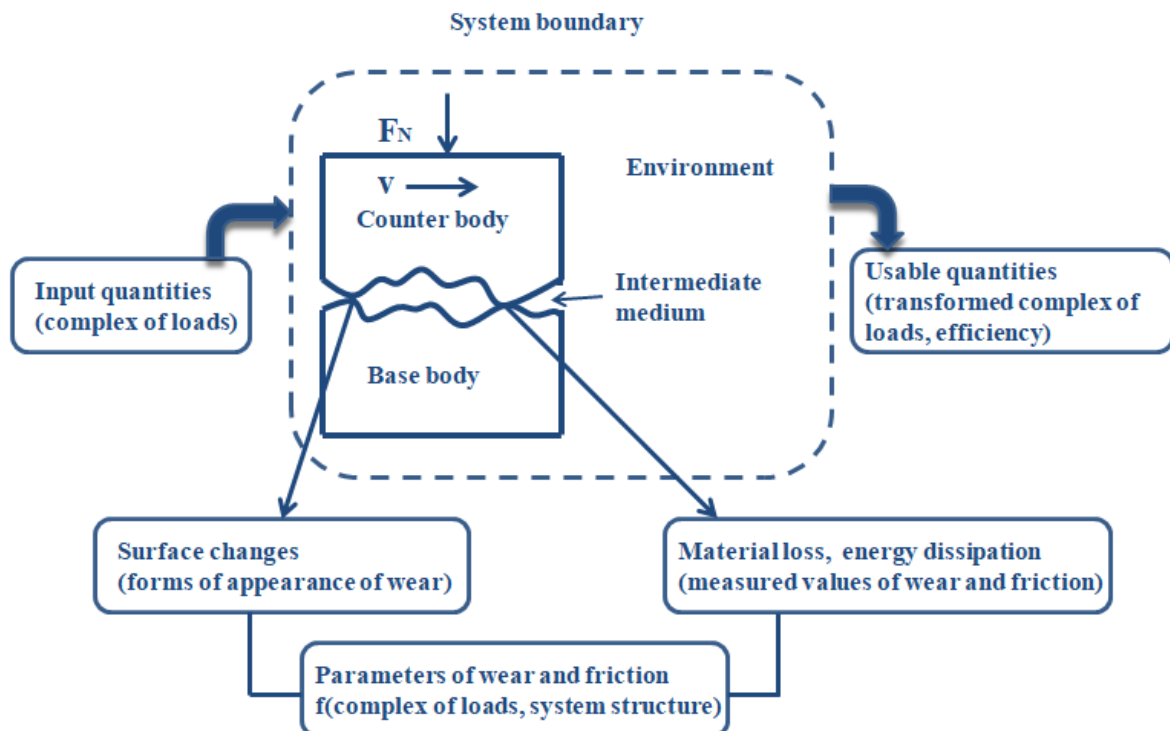


Figure 2: Representation of a tribological system adapted from [7].

2.1.3 Friction conditions

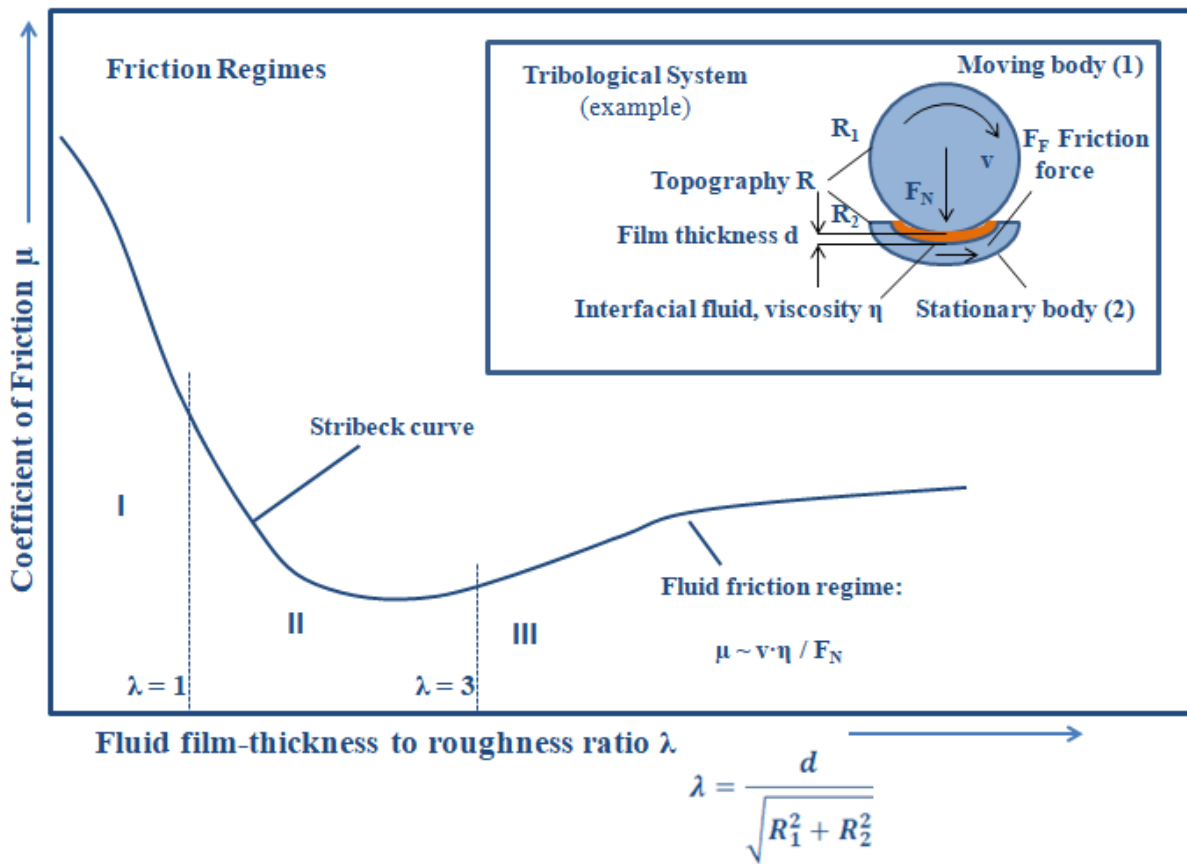


Figure 3: *Stribeck* curve adapted from [10]

The *Stribeck* curve as depicted in Figure 3 describes the dependency of the value λ , which stands for the ratio of fluid film-thickness to the roughness, on the COF.

This curve can basically be categorized in 3 areas. Area 1 includes the condition of solid friction, which is actually located on the y-axis, because there is no fluid lubrication in between solid-solid contact. It also comprises the condition of boundary friction up to a value of $\lambda=1$, in which the COF decreases due to molecular interface-layers. Area 2 is between a λ value of 1 and 3 and describes the condition of mixed friction, where the fluid film is not yet thick enough to separate both friction partners uninterruptedly. In this area, solid contact and fluid friction coexist and the COF reaches its minimum. The third area pictures the zone of fluid lubrication, in which the COF starts to increase again due to internal friction. In this area the COF is dependent on the Hersey number, which is defined as $v \cdot \eta / F_N$ (where v is the velocity, η is the viscosity and F_N is the normal load).

The different forms of contacts and the therefore resulting different friction and lubrication conditions are described in the following:

- **Solid friction (dry friction)**

This type of friction describes direct solid-solid contacts without any separating layer. The COFs and wear rates of conventional materials are high and lubrication techniques try to minimize these values [7, 11].

- **Boundary friction**

In contrast to solid friction the surfaces in boundary friction are covered with friction-reducing, molecular interface-layers. These films can be created by surface active substances via adsorption, tribochemical reactions and chemisorptions. It is a main target of lubrication to create such kind of layers in order to influence friction and wear and they are the method of choice, when other films, which separate two surfaces, are technically impossible to achieve [7, 9, 11].

- **Mixed friction**

The coexistence of boundary friction and fluid film friction is called mixed friction [9]. The lubricating film is not thick enough to completely separate the two surfaces from each other and therefore the load is partially absorbed by the lubricating film as well as by the other roughness contacts [11]. The *Stribeck* curve and underlying research [12], which is usually attributed to the german engineer *Richard Stribeck*, is a graphic illustration of the friction conditions and was firstly developed in 1902 [13]. However basic work and experimental exploration in this field was done even earlier [10].

- **Fluid film friction**

In fluid film friction both friction partners are completely separated by a hydrodynamically or hydrostatically generated fluid lubricant film. The frictional resistance conditioned by the rheological properties of the fluids causes liquid or fluid friction. If the separating film is an aerodynamically or aerostatically formed gas film, it is common to name it as gas friction and gas lubrication [7].

2.1.4 Types of friction

Regarding tribotechnical applications, it is common to subdivide friction according to kinematics. A distinction is made between the following main types of friction in respect of the type of relative movement of the contact partners.

- **Sliding friction**

Sliding friction is linked with relative translational movement of touching material areas. It is of major importance in technology and relevant for the performance of various tribotechnical systems. A classic machine element, where sliding friction occurs, is the sliding bearing [9].

Drilling friction is a special type of sliding friction regarding bodies, whose rotation axis is perpendicular to the contact area and whose movement is only about this axis, while there is macroscopically a steady state of the contacting area in the reference area. Phenomenologically it can be understood as sliding friction with a velocity gradient from the middle of the rotation axis in radial direction up to the edge of the contact area [9].

- **Rolling friction**

This type of friction is generated by rolling contact. A roller is a rotating body with a rotation axis parallel to the contact area and a movement perpendicular to the axis. Rolling movements are of great importance, because their friction resistance is much smaller than those of sliding movements. The main reason for this fact is that during rolling processes the contact areas of two partners are only approaching and leaving the contact area vertically. Sliding processes however involve shear stresses to a large extent. Roller bearings are a well known example for this friction type [9].

- **Stick-slip**

Stick-slip often occurs in slow sliding friction, especially when the static friction coefficient is greater than the dynamic friction coefficient and the friction partners are coupled to a vibrating system. The reason for this effect are, to be specific, self-excited friction vibrations [11]. The friction partners are coupled to a vibrating system. Surface adaption or additives in lubricants can lower the effect of stick-slip [7, 9].

2.2 Wear

Wear is defined as the progressive loss of material from the surface of a solid object due to tribological stresses [9].

2.2.1 Wear mechanisms

Wear mechanisms describe the physical and chemical interactions in the contact area of a tribological system. They trigger elementary processes and result in a material and shape change of the tribologically stressed samples. Starting in the microcontacts, their contribution to wear depends on the load spectrum and the shape of the tribological system. Wear is mainly determined by four different wear mechanisms, which usually do not occur alone, but often superimpose and may intensify each other:

- **Adhesion**

Adhesion is a material interaction at molecular and atomic levels. Materials have a certain degree of roughness and therefore, if a tribopair comes into contact, it actually means that only the peaks are in direct contact. Due to mechanical stresses and relative movement elastic and elasto-plastic deformation may take place and result in the destruction of superficial layers. In combination with local high temperatures at the micro contacts by reason of the transformation of frictional energy, this interplay can lead to the creation of atomic bonding between two materials. In the case of metallic contact partners this bonding is called “cold welding” [9]. Depending on the strength of the bonding the two materials now can separate either in the original contact zone or below the surface of a contact partner having the weaker cohesion, which results in a transfer of material from one object to the other.

Adhesion plays a great role in a tribological system containing two materials of similar hardness [7].

- **Abrasion**

In contrast to adhesion abrasion is predominant in tribo systems with friction partners of different hardnesses. The harder material has an abrasive effect and penetrates the surface of the softer object. Relative motion therefore results in scratches and can even lead to material breaking away and causing severe wear. Abrasion is linked to 4 different interaction processes, which normally occur at the same time [7]:

Micro-plowing: The material experiences plastic deformation by the harder abrasive acting counter-part and is piled-up at the edges. Micro-plowing does not necessarily include material abrasion [7].

Micro-cutting: In ideal micro-cutting the abrasive part creates a micro-shaving right in front of itself with exactly the same volume as the arisen wear tunnel [7].

Micro-fracture: Supercritical loads on materials cause the formation and propagation of cracks, which can finally result in material breaking away. Brittle materials are particularly endangered [7].

Micro-fatigue: This is strictly speaking part of surface fatigue and occurs within repeated micro-plowing leading to local material fatigue processes and material abrasion [7].

In the likely case of superposition of more processes it is useful to introduce the so-called f_{ab} value that describes the relative partial processes of micro-plowing ($f_{ab} = 0$) and micro-cutting ($f_{ab} = 1$) [7].

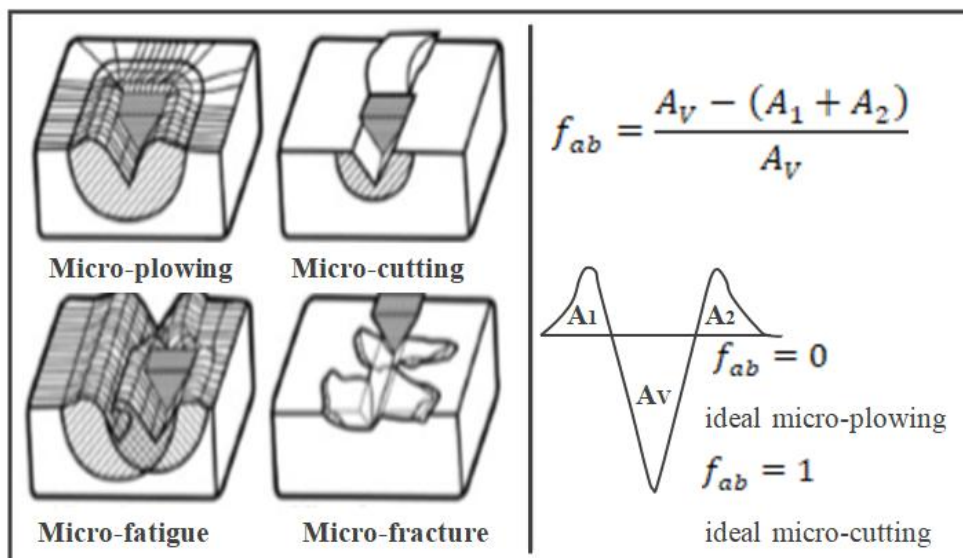


Figure 4: Detailed abrasion processes adapted from [7]

Figure 4 illustrates the different wear mechanisms on the left and shows how the f_{ab} value is determined on the right. A_V is the cross section of the wear groove, A_1 and A_2 are the piled up cross sections caused by micro-plowing.

▪ **Surface fatigue**

In a tribological system, forces are absorbed by the contacting surfaces, which, considering the relative movement, cause a material strain. Especially in periodically loaded areas of the micro-contacts, such as in Hertzian contacts, damage accumulation or material fatigue can occur, leading ultimately to the formation of cracks and their spreading. Compared to volume-based fatigue the penetration depth of the loads is only acting on the edge of the material.

In general, material fatigue is determined by load amplitude and number of cycles. In short-term fatigue quasi-static fracture can occur at load amplitudes corresponding to the tensile strength. However, long-term fatigue is rather associated with low load amplitudes. Depending on the number of load cycles, the fatigue process can be split into the following steps with respect to the development of the altered microstructure: 1) incubation period (accumulation of lattice distortions and errors), 2) creation and development of submicro cracks to micro cracks, 3) crack spreading and crack association 4) final fracture.

J. Halling developed a numerical model for the wear volume caused by the surface shattering mechanism [14].

▪ **Tribochemical reactions**

Tribochemical reactions describe chemical reactions between a tribo-body and the ambient medium and/or the intermediate material. In contrast to corrosion these reactions only take place at the contact surfaces during relative motion.

Surface areas adjacent to the contact areas have an increased chemical reactivity as a result of thermal and mechanical activation due to friction processes. As naturally appearing reaction layers are broken due to mechanical loading, high-energy surface zones become exposed. This leads to higher capacities of surfaces to start a chemical reaction, tribochemical reactions in this case. The reaction products have generally different properties and therefore an influence on the behavior of friction and wear. A prime example is the formation of metaloxides in metallic contact points. These oxides have a tendency to brittle breakout as they are less able to reduce mechanical stresses through plastic deformation. Such coatings can also have a wear-reducing effect if they prevent direct metallic contact between the base body and the counterbody and thus adhesive wear. Humidity of the ambient medium also has a big influence [7, 9].

T.F.J. Quinn used his publication about the role of oxidation in the mild wear on steel to develop a model for the wear of tribochemically created reaction layers [15].

2.2.2 Wear parameters

In order to be able to measure wear and express it in numbers, there are two main types of term.

- Wear parameters describe the change of shape and mass of a body by means of measured values.
- Wear appearance forms describe the change of the surface as a result of tribological stress and the type and shape of the wear particles.

There is a distinction made between direct and indirect wear parameters. While direct parameters describe the change to the form or mass of a component, indirect parameters are set in relation to a reference value, like velocity, distance, or throughput. In this respect we are talking about different kinds of “wear rates”. Besides different possibilities to describe the wear rate, there is a worldwide used wear coefficient, which results from an adaptation of the *Archard* equation from 1953 [16] and is standardized to the load [9].

$$k = \frac{W_v}{F_N \cdot s} \quad (1)$$

k = wear coefficient (m^2/N)

W_v = wear volume (m^3)

F_N = normal load (N)

s = sliding distance (m)

The macroscopic parameter k indicates the volume loss per load unit of a tribological system occurring under a constant load after a certain sliding distance (not rolling), assumes a proportional relationship between the wear volume, the sliding distance and the load unit and is widely used due to the fact that it makes wear results obtained by different geometries, densities, loads and test times comparable. Basically, it is only used in the area of solid body friction and mixed friction. When comparing values, care should be taken to ensure that friction conditions and wear intensities were determined for similar pressure, load and temperature ranges.

It is also noteworthy that the wear coefficient does not contain any information about the wear mechanism. Apart from that it is not a material constant, since wear results from interaction processes of contacting bodies and must always be related to the tribological system. In order to be able to clearly identify a result, it is therefore necessary to declare the wear data of both contact partners or of the entire system individually. Due to their complexity, wear parameters generally cannot be calculated and must instead be determined experimentally and presented in a meaningful form.

In the original equation, the wear rate k is multiplied by the room temperature hardness of the softer friction partner, so that a dimensionless quantity K is obtained [9].

2.3 Friction modification

2.3.1 Dissipation of friction energy

Energy dissipation describes the conversion of mechanical kinetic energy into other forms of energy. The main process of frictional energy dissipation is the conversion into heat. In addition, energy dissipates as mechanical vibrations via materials directly connected to the friction bodies. The other two processes are energy absorption and energy emission [9].

Energy absorption

Since friction mechanisms are associated with the generation of lattice vibrations, elastic contact deformation creates and reduces stress fields and thus vibration fields. It has been shown that in areas of plastic contact deformation in the contact areas lattice defects are generated and moved through the lattice. Adhesion bonds of microscopic contact surfaces, which are separated, manifest themselves as deformation and generate waves and atomic movements of the lattice building blocks. In a simplified way, the energy losses caused by contact deformations can be divided into a few main mechanisms:

- Dislocations that move require a certain energy that is released when they are blocked.
- Energy is continuously dissipated from dislocations as these thermoelastically attenuate and scatter acoustic waves.
- During deformation, dislocation lines are created and destroyed.
- During the deformation, spot defects are generated and destroyed.

It has been experimentally confirmed several times that friction in metallic solids is associated with an increase in dislocation density. However, the friction energy absorbed by dislocation mechanisms is estimated to be less than 1 % [9].

Energy emission

Triboemission processes can play a significant role in tribochemical reactions [17]. Apart from frictional electricity, the emission of sound, photons, ions and electrons is also important for the frictional energy emission.

- Sound emission/Phonon emission

The emission of acoustic waves and the associated noise development is a well-known friction effect and is generated by forced and elastic oscillations through movements of components in the tribocontact. These oscillations excite the air particles, which oscillate in the entire audible frequency range.

- Photon emission (triboluminescence)

Emission of optical radiation due to friction can occur far below temperatures of thermally induced emission. Triboluminescence is particularly observed in the friction and fracture of crystals and is physically explained by the friction-induced mechanical activation and the associated excitation of electrons near surface atoms. The recombination and the return to the ground state results in the emission of optical radiation.

- Electron- and ion emission

Similar to triboluminescence electrons are excited to emit from the friction partners by converted friction energy. The frictional electron emission can be classified as follows.

- Mechanically induced emission: mechanical interactions in tribo-contacts cause defects in the friction partners, which are connected with additional energy levels from which electrons can be emitted.
- Mechanically-optically induced emission: If surface cover layers of the contact partners are shifted by tribomechanical stress, free surfaces can be formed for a short time, which emit electrons when exposed to light.
- Chemo-emission: Through adsorption processes, an electron emission takes place on a freshly formed surface.

- Thermal emission: At locally very high temperatures, an emission of thermally induced electrons is possible.
- Field emission: Charge separation, which can be caused, for example, by a fission process, can generate the field strength required for a field emission [9].

2.3.2 Anticipating friction

There are several different approaches of anticipating the friction. This chapter is supposed to give an overview about the most common methods.

Lubrication and additives

Lubrication is a very efficient way to reduce friction and wear, thereby increasing the service life of materials. In principle, during lubrication, the contact surface of two friction partners is reduced or completely separated with the aid of a lubricant. Apart from this task, lubricants can also have a sealing effect, can help to dissipate heat, remove wear particles or prevent corrosion [11]. Additives are often added to lubricants to ensure required properties and influence the performance of the lubricant. The *Stribeck* curve in Figure 3 gives a description of the possible friction conditions in lubrication.

While liquid lubricants are paid much attention, there are also solid lubricants. The most popular ones are MoS₂, Graphite and PTFE [11].

Surface adaption

Modifying the surface of tribologically stressed materials is another way of adapting the friction and is proven to be effective at lowering friction [18, 19]. The aim of this concept is to create well-defined surface topographies such as dimples, bumps and lattice like pattern geometries, which can be responsible for reducing the contact area or trapping wear particles. Possibilities to realize this task are honing, micro coining, lithography or laser surface texturing [20].

Coatings

Coating is a manufacturing process in which a firmly adhering layer of formless material is applied to a material [21]. There are a variety of functions for coatings. From a tribological

point of view, however, the possibility of applying more wear-resistant, harder or friction-reducing coatings on a substrate plays the most important role.

Design

With the design of materials, the friction coefficient can also be significantly influenced without additional substances. Good examples of successful, friction-reducing design are different types of bearings.

Material selection

A relatively simple and obvious possibility to change the friction is the material selection. Steel on steel has a different coefficient of friction than steel on aluminum [22]. Other material combinations, which nevertheless fulfill all other requirements, can save complicated processes.

Another option to anticipate friction is the formation of **tribofilms**. The following chapter is dedicated to the fundamental importance attached to this possibility in relation to this work.

2.3.3 Tribofilms

There is no uniform definition of the term tribofilm and there is also research work, in which this term is described under another name like boundary film [23], boundary lubricant film [24], boundary lubricating films [25] or tribo-boundary film [26]. However tribofilms are referred to reaction layers that are formed in tribological systems in an interaction between a friction surface and the chemical components of a lubricant [27] and were firstly discovered by *Bowden* as he described reaction layers in boundary lubricated metal contacts [28]. Figure 5 shows how it is imagined that tribofilms are formed and lists important parameters for their formation.

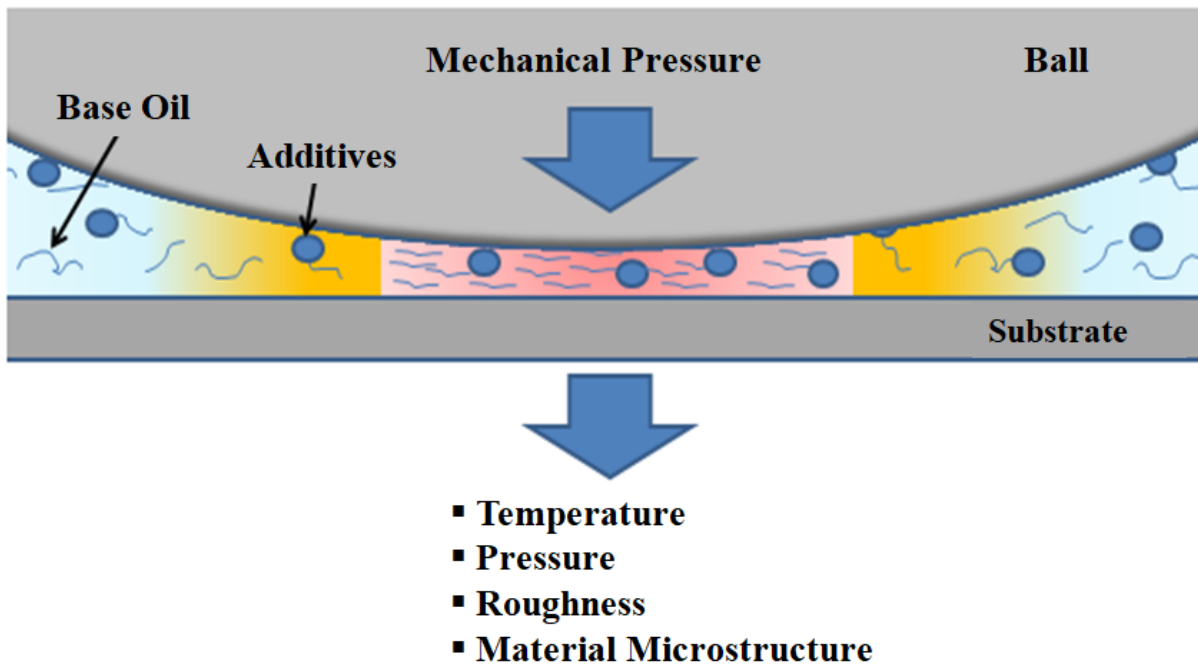


Figure 5: Reasons for tribochemical reaction

Figure 5 is intended to illustrate that the reasons for a tribochemical reaction are diverse in nature and to highlight the complexity of this process. Tribofilms can be generated mechanically, chemically and thermally [29]. The idea is that additives in lubricants react in different ways with the surface material and influence the friction behavior. A major reason why it is worth investigating the mechanism and growth of tribofilm formation is that tribofilms can show friction and wear-reducing effects [4] and are a way of separating two contact surfaces in boundary lubrication. Tribofilms can therefore be used as an interface medium to prevent wear on the actual surface of the material. Additives for tribofilm production can be classified according to their chemical reaction mode: There are additives that react directly with the surface material and additives that can form tribofilms by thermal or oxidative reactions without surface sacrifice [24]. 2 very intensively investigated substance classes, which are considered suitable for the formation of tribofilms, are presented below.

ZDDP-tribofilms

Zinc dialkyldithiophosphates (ZDDPs) have their main application as additives in lubricants and engine oils, in which they can act as an antioxidant or corrosion inhibitor, but above all they have an anti-wear effect [4, 30, 31]. Figure 6 shows the structural formula of ZDDP.

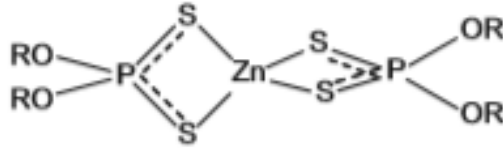


Figure 6: Structural formula of ZDDP [32]

ZDDP is known to form tribofilms under mechanical shear stress and/or thermal activation. To be effective, ZDDP must be in dissolved form. It can react with radicals and thus inhibit oxidation. If ZDDP is rubbed on iron surfaces, wear-reducing ortho- and pyrophosphate-based tribofilms can form. Apart from this, ZDDP can form metal sulfides and absorb wear particles consisting mainly of iron oxide [30, 33, 34]. The shear stress, however, controls the rate of formation of the tribofilm [4, 30]. This “thick, phosphate glass-based” [32] tribofilm is the main reason for wear limitation.

Ionic liquid tribofilms

Ionic liquids (ILs) are usually referred to large salts, which resist crystallization at low temperatures, have diffuse charge and tailored properties [35]. Their possible use in lubrication has been investigated since 2001 [36]. Similar to ZDDP it is possible to create tribofilms with ILs. The combination of ILs and ZDDPs was also investigated [37].

2.4 Chemistry of the precursors

The idea behind the application of the following precursors was to generate wear-resistant layers/films in friction contacts by means of their activation and reaction with the substrate. The assumption is that these compounds can form tribofilms and/or form ceramic-like layers by decomposition and reaction, because the precursors are organosilicon compounds and their polymers can be used as starting materials for the production of ceramics (polymer-derived ceramics PDCs). This process usually consists of the following steps: shaping, cross-linking, pyrolysis and crystallization. Figure 7 provides an overview of the polymer classes that can be used as starting materials for the respective ceramics.

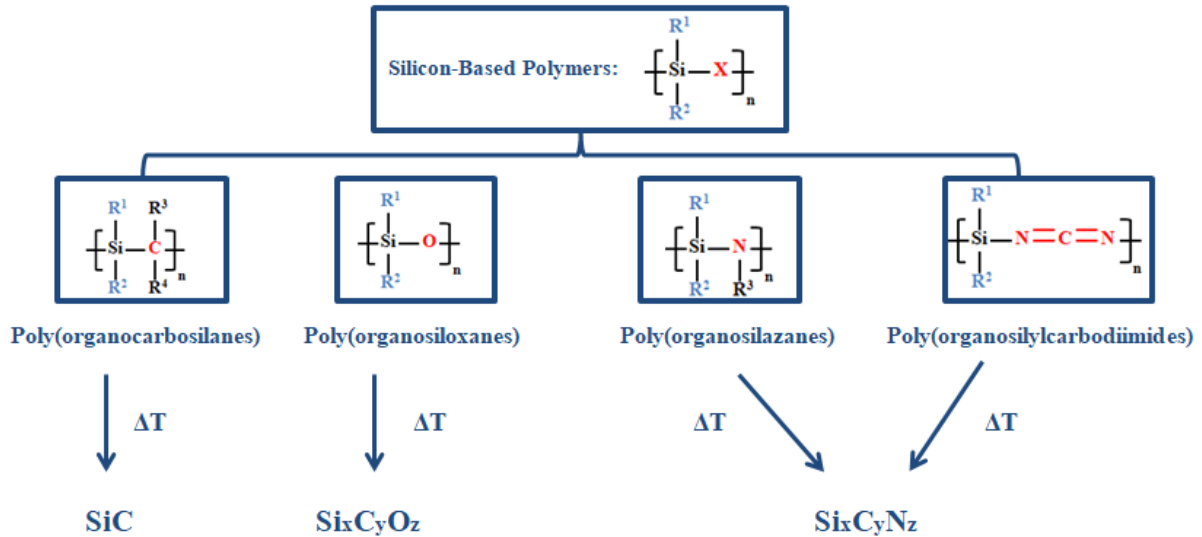


Figure 7: Possible ceramic reaction products of organosilicon polymers after thermal decomposition adapted from [6]

2.4.1 Bis(trimethylsilyl)carbodiimide (precursor 1)

Bis(trimethylsilyl)carbodiimide (BTSC) is a colorless liquid that can be mixed with diethyl ether, dioxane, carbon tetrachloride, benzene and petrol [38]. At room temperature it is considered as stable, but flammable [39]. Figure 8 shows the structural formula of Precursor 1.

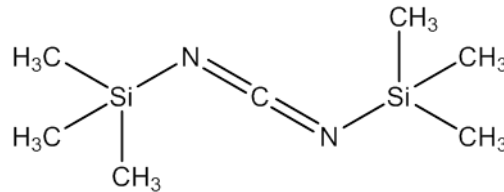


Figure 8: Structural formula of bis(trimethylsilyl)carbodiimide

Table 1: Important physical data of precursor 1

Melting point	Boiling point	Flash point	Molar mass	Density (25 °C)
-23 °C	164 °C	21 °C	186,4 g/mol	0,8211 g/cm ³

Table 1 shows the most relevant physical data of precursor 1 [39].

BTSC is considered an interesting chemical in terms of tribology, as it is possible to produce smooth and hard Si/C/N coatings with excellent corrosion properties [40].

2.4.2 Poly(methylphenyl)siloxane (precursor 2)

Poly(methylphenyl)siloxane is a colorless liquid.

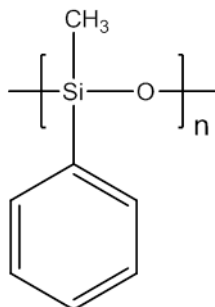


Figure 9: Structural formula of poly(methylphenyl)siloxane

Table 2: Important physical data of precursor 2

Melting point	Boiling point	Flash point	Molar mass	Density (25 °C)
-	-	225 °C	-	1,102 g/mL

Table 2 shows the most relevant physical data of precursor 2 [41].

2.4.3 Trimethoxyphenylsilane (precursor 3)

Trimethoxyphenylsilane is a flammable liquid.

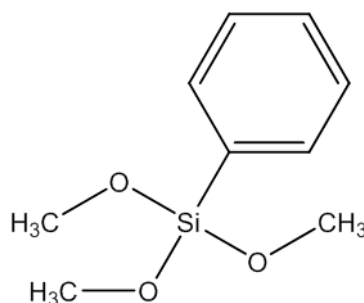


Figure 10: Structural formula of trimethoxyphenylsilane

Table 3: Important physical data of precursor 3

Melting point	Boiling point	Flash point	Molar mass	Density (25 °C)
-25 °C	233 °C	29 °C	198,29 g/mol	1,062 g/cm ³

Table 3 shows the most relevant physical data of precursor 3 [42].

There are scientific publications in which the friction-reducing effect [43] and the use of trimethoxyphenylsilane as a lubricant [5] is described.

3 Methodology

The following chapters describe the instruments that were used in order to carry out the experiments and analyzing them. There was a big focus put in the analytical methods.

3.1 Tribometer

A tribometer is a device for measuring frictional forces. Depending on the task there are many different types. The experiments within this thesis were carried out with the help of a SRV (Schwing-Reib-Verschleißprüfgerät), which is a high-frequency, linear oscillation test machine and is used for simulating very low displacements. It is primarily used for investigation of scuffing phenomena appearing in automotive elements, aircrafts and machines, which vibrate. In this work the main task was the determination of the friction coefficient μ . The base body in general is a disc and the counter body, which can be a ball, a cylinder or a ring, oscillates translatorily at a defined normal load, frequency and path length on it. Apart from load, frequency and path length there is also the possibility to vary the temperature and the atmosphere or humidity at different tests. A SRV is capable of performing systematic property studies in an easy and fast way without needing a big amount of lubricant. Figure 11 illustrates the test chamber of a SRV with all necessary components.

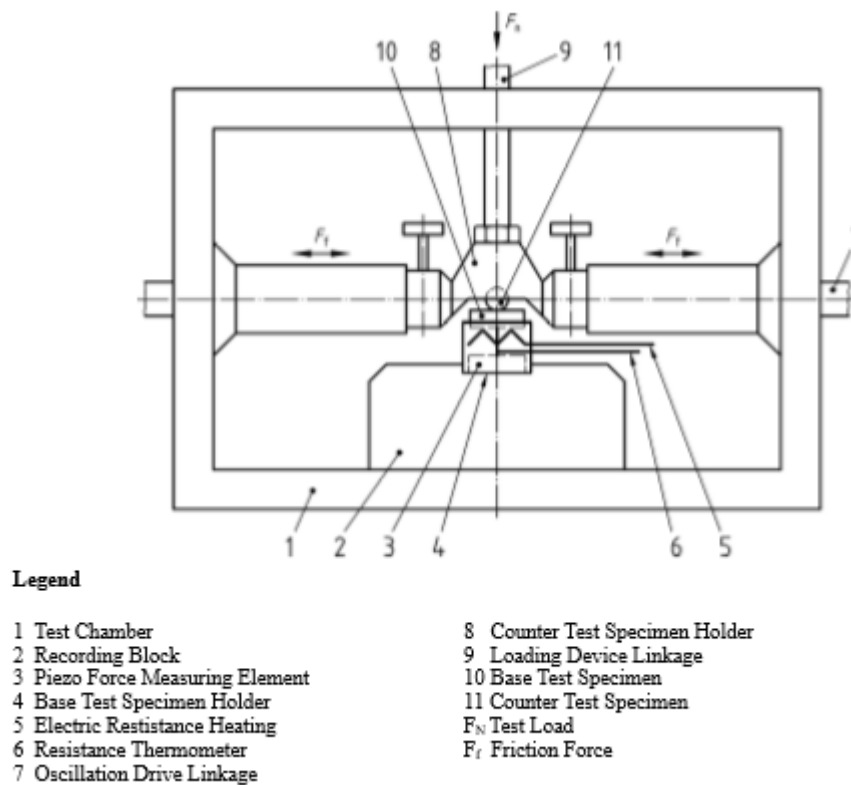


Figure 11: Schematic of the Test Chamber adapted from [44]

3.2 Confocal microscopy

A confocal Microscope is a special type of light microscope. It can reduce light, which is out of focus and increase the signal-to-noise ratio compared to bright-field methods. The basic principle is that excitation and detection are focused onto the same region of the sample, which is diffraction limited. The term confocal is derived from this idea. There is also a pinhole placed in the image plane of the specimen to make sure that only light from a small part of the sample reaches the detector. Due to the limited region of the sample, which can be observed at one point at a time it is necessary to record an image [45].

One special design of confocal microscopes is the differential confocal microscope (DCM), which was mainly used in this work with the purpose of determining wear volumes. The LEICA DCM 3D instrument has a measuring head, which moves in a vertical direction and records the intensity curve for each measuring point as a function of the traverse path; a 3D surface image is generated from the pointwise position of the maxima. There are no mechanical or rotating parts for x/y-scanning, only slits have to be stepped through the field, so not only one point is illuminated but multiple lines. With the use of a charge-coupled device (CCD), pixels at the right positions can serve as pinholes and photodetectors.

3.3 Scanning electron microscopy and energy-dispersive X-ray spectroscopy

3.3.1 Scanning electron microscopy

A scanning electron microscope (SEM) is a type of electron microscope that creates magnified images of a surface by scanning it with a focused electron beam under high vacuum. With regard to the type of electron emission, a distinction is made between thermionic and field-emission SEMs. In thermionic SEMs, the electron emitter consists of a tungsten cathode or a LaB₆ filament. For field-emission SEM there are the variants with a Schottky emitter, which strictly speaking is a field-supported thermionic emitter, and cold field emission SEMs. The electrons are accelerated through a voltage potential and focused on the sample via lenses, apertures and coils. The rastering over the surface and the interaction with the examined specimen leads to different signals, which contain information on the shape, composition, crystallography and other properties. The emitted signals are detected and the detector creates an image in collaboration with the software [46, 47].

Main parts of modern SEMs are an electron optical system, a vacuum system, an electronic system and a computer with software. The electron optical system consists again of an electron gun, a demagnification system, a scanning unit and a focusing system [47].

Considering the signals there are two outgoing electron products of great importance, which are called backscattered electrons (BSEs) and secondary electrons (SEs). BSEs are beam electrons, which experienced scattering and deflection by the electric fields of the sample atoms and have completely reversed their initial direction. The energy of these electrons is diminished due to inelastic scattering. BSEs can be quantified with the “backscattered electron coefficient” η , which is defined as $\eta = N_{\text{BSE}}/N_{\text{B}}$ where N_{B} is the number of beam electrons that enter the sample while N_{BSE} describes the emerging backscattered electrons. This coefficient gets higher with atomic numbers and that is why heavy elements appear brighter on BSE images than light elements [46].

SEs are due to inelastic scattering of the electron beam ejected valence electrons (ionically or covalently bound materials) or conduction band electrons (metal). Similar to BSEs they can also be described by a parameter $\delta = N_{\text{SE}}/N_{\text{B}}$, which is the ratio of SEs emitted from the sample, N_{SE} , to the number of primary beam electrons N_{B} . A characteristic feature of SEs is their very low kinetic energy. The big mismatch between the kinematic energy of the primary beam electrons (1-30 keV) and the weakly bound atomic electrons (1-15 eV ionization energy) results in a small energy transfer. Additionally the created SEs have to propagate to the surface and experience inelastic scattering, which is also lowering their energy. Since SEs that are close to the surface are therefore in advance and have better chances to escape from the sample, SE images are often used to get information about the topography of a surface [46].

The following figure shows the possible signals that can be generated by the interaction of an electron beam with matter.

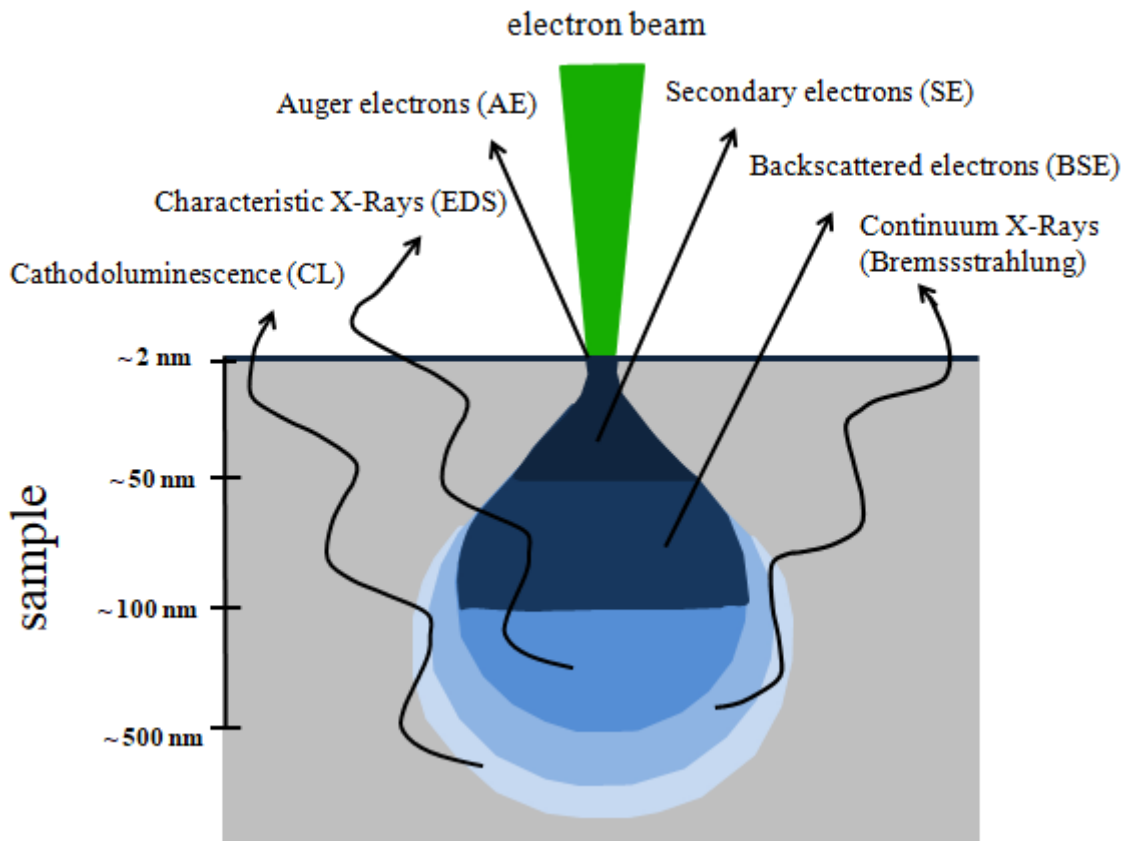


Figure 12: Electron beam interaction with the sample adapted from [48, 49]

The shown signals in Figure 12 are all described in this or the following chapter except cathodoluminescence (CL). This effect, which plays only a subordinate role in classical SEM, describes the emission of light and is also generated by an electron beam.

3.3.2 Energy-dispersive X-ray spectrometry

Energy-dispersive X-ray spectroscopy (EDS) is a type of X-ray spectroscopy, which is very often combined with a SEM. EDS systems usually comprise an X-ray detector, a pulse processor and an analyzer. In this case, atoms of the sample are excited by an electron beam. The knocking out of electrons close to the nucleus causes a vacancy and results in an unstable state, which is compensated by the reoccupation of higher-energy electrons from higher atomic orbitals. The energy difference becomes free in the form of an X-ray quantum and is element-specific. Depending on the shell from which the energy-rich electron originates and the shell from which the energy-poor electron was knocked out, X-ray quanta of different energy are produced. The occurring peaks in the spectrum are named after the shell, from which the energy-poor electron was knocked out (K, L etc.) and the shell, which the energy rich electron left in order to reoccupy the arisen gap (α , β etc.). In addition to the element-specific peaks, the spectrum also consists of an unspecific background generated by Bremsstrahlung [47]. However, this process is in competition with the Auger effect, in which

the energy released is not emitted by X-rays, but is transferred to a weakly bound electron, which is then emitted as an Auger electron. This effect is applied in so-called Auger electron spectroscopy (AES).

The analyses within this work were carried out with the help of a FEI Quanta 250 FEGSEM.

3.4 Raman spectroscopy

Raman spectroscopy is one of the most important methods of vibrational spectroscopy. It is a surface sensitive, non destructive method to identify molecules by their spectra, interpreted like fingerprints. It relies on irradiating a sample with monochromatic coherent or non-coherent radiation usually from a laser between the ultraviolet and near-infrared range and inelastic scattering. Vibrations are raman-active, only if the molecular polarizability is modulated by the vibration [50].

There are two different kinds of scattering, which might happen, if a light quantum $h\nu_0$ hits a molecule. The most probable one is called Rayleigh scattering and stands for elastic scattering. The opposite inelastic effect goes with an exchange of vibrational energy and is called Raman scattering. The emitted energy after this process can be described as $h\nu_0 \pm h\nu_s$. It therefore can be higher or lower than the energy of the initial light quantum. The Boltzmann's law tells us that at room temperature most of the molecules are in their vibrational ground state, not in their excited state. Due to this fact the transfer of vibrational energy to a molecule is more likely to occur than the reverse process and this leaves a quantum of lower energy $h\nu_0 - h\nu_s$. George Stokes discovered in 1852 that the wavelength after fluorescence is always longer than of the absorbed light [51]. Lines are therefore referred to as Stokes lines and anti-Stokes lines and are caused by quanta of lower and higher energy respectively. The difference between absorbed and emitted wavelength is called Stokes Shift. As a result of their unequal probability Stokes lines have higher intensities and are usually recorded as Raman spectrum. The elastic scattered irradiation is usually filtered out, while the rest of the light is recorded by a detector [50]. Figure 13 shows the different processes of light scattering.

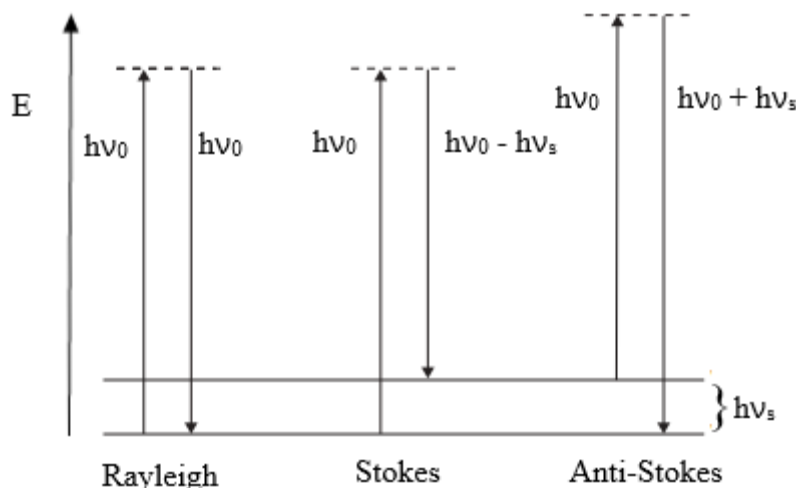


Figure 13: Possible scattering processes for light quanta adapted from [52]

There are many variations in terms of geometry and also of components concerning the construction of a Raman spectrometer. Main components however include a laser source, collection optics, a wavelength analyzer, a detector and a computer [53].

Raman spectroscopy is used within this work to identify functional groups and molecules of the potentially created tribofilms. A WITec alpha 300 RSA+ device was used with the parameters shown in the following table.

Table 4: Parameters for Raman analysis

Wavelength	Laserpower	Grating	Magnification	Accumulations	Integration time
532 nm	2 mW	600 g/mm	100x	50	1 s

3.5 Focused ion beam

The Focused ion beam (FIB) is a notable instrument for manipulating and also understanding the structure of materials. This at nanoscale working tool has basically four different ways of operating: milling, deposition, implantation and imaging. It has similar imaging capabilities to SEM and in addition to that it is also a very precise machining tool and is able to adapt the surface of materials. In contrast to SEM that is based on the application of an electron beam, FIB uses a stream of high-energy ionized atoms that are created by a liquid-metal ion source. The ions are focused into a beam by an electric field, pass through apertures and are scanned over the surface of a specimen. The use of relatively massive elements like Gallium allows the ion beam to expel surface atoms easily while creating secondary electrons and therefore imaging the sample before, during and after other executing processes [54].

Ion beams are much larger and can be positively charged compared to electron beams. Ions also have a smaller penetration depth and are more likely colliding with atoms than electrons. The ionization of surface atoms and the breaking of the bonds between them are therefore the main interactions. Obviously the use of an ion beam can often result in unwanted damage to the sample. Due to high sample complexity and some disadvantages of this tool, a very common dual beam method has been developed, which combines the powerful, large and massive ion beam of the FIB with the less destructive, high-resolution electron beam of the SEM [54]. The dual beam technology is useful particularly for cross section preparation using the electron beam for imaging while the ion beam is milling [55].

3.5.1 Preparation of a TEM-foil

The preparation of a TEM cross section can be done in different ways, but in a simplified way this process includes the following steps: Platinum is deposited at the top of the surface of the desired cross section as a protection layer. Within a milling process the material surrounding the cross-section is removed. The produced foil is then lifted out using a micromanipulator and welded to a copper lattice with platinum. Afterwards the final thinning takes place via ion beam.

FIB technique was primarily used in this work in order to prepare a section, which can be used for following TEM analysis and further to get additional information to the results, which were obtained with SEM. A FEI Quanta 200 3D DBFIB was used for that purpose.

3.6 Transmission electron microscopy

A transmission electron microscope (TEM) is a type of electron microscope. A major difference to the SEM considering sample request is that sufficiently thin samples are required, so that they are permeable to electrons. The necessary thickness depends on the atomic number and the accelerating voltage. There are different versions of TEMs, but in general they use a high-energy electron beam for probing the sample and collect the forward scattered electrons. The two basic operating modes include diffraction and imaging. Electrons with parallel trajectories after passing the sample, like those scattered from a row of crystalline planes are brought to a focus in the focal plane of the objective lens, the reciprocal space. The resulting diffraction pattern contains information about the spatial frequencies of the sample. The trajectories of the electrons recombine while propagating to the image plane of the lens, giving a real space, slightly magnified, inverted picture of the sample [56].

There are two different imaging techniques: In the more common bright-field (BF) technique the central unscattered beam is selected by an aperture in the back focal plane of the

objective lens, while the diffracted beams are excluded. The dark-field (DF) imaging however only selects a chosen reflection and that is why only regions in the crystallographic orientation appear bright on a dark background [56].

The basic instruments generally consist of an electron gun, apertures and probe-forming lenses, a vacuum system, a specimen holder, image-forming lenses and apertures and electron detectors [56].

The idea of TEM-application in this work was to characterize possibly formed tribofilms. The analysis was carried out with a FEI TECNAI F20.

3.7 X-ray photoelectron spectroscopy

X-ray photoelectron spectroscopy, which is more commonly referred to as XPS, is a widely used surface sensitive analytical method and is based on the photoelectric effect that Albert Einstein explained in 1905 [57]. In this analytical method the sample is irradiated with soft X-ray photons. These photons have a defined energy of $h\nu$ and can transfer their energy to electrons of the sample with binding energies of E_B . If the energy of the X-ray photon exceeds the binding energy of an electron, this electron gets ejected from the matter to the vacuum and is called photo electron. The kinetic energy of an ejected electron is measurable in XPS and can be described by formula(2 [58].

$$E_{Kin} = h\nu - E_B - \Phi_S \quad (2)$$

E_{Kin} = kinetic energy of ejected electron

$h\nu$ = photon energy

E_B = binding energy of electron

Φ_S = work function of spectrometer

In XPS the attention is usually focused on electrons from core levels, although they may also originate from the valence band. Two elements do not share the same set of electronic binding energies and that is the reason why XPS makes elemental analysis possible. The chemical environment of an atom has an influence on its binding energy and therefore chemical information can also be obtained by XPS. Apart from Hydrogen and Helium, whose cross section is too low, basically all elements of the periodic table can be detected. The only requirement to the sample is that it has to be compatible with ultra high vacuum [58].

Beside the photo electrons there are two more signals, which are worth mentioning and already have been described in chapter 3.3 Scanning electron microscopy and energy-dispersive X-ray spectroscopy. The ejected photo electron leaves a core vacancy in the atom, which can get reoccupied by an electron transition from a higher shell. The energy difference between the higher shell and the core shell can now either be dissipated as an X-ray photon or an Auger electron. These signals can be useful, however they are not a central part in XPS [58].

XPS is a very surface-specific analytical method and the reason for this can be explained by the following figure.

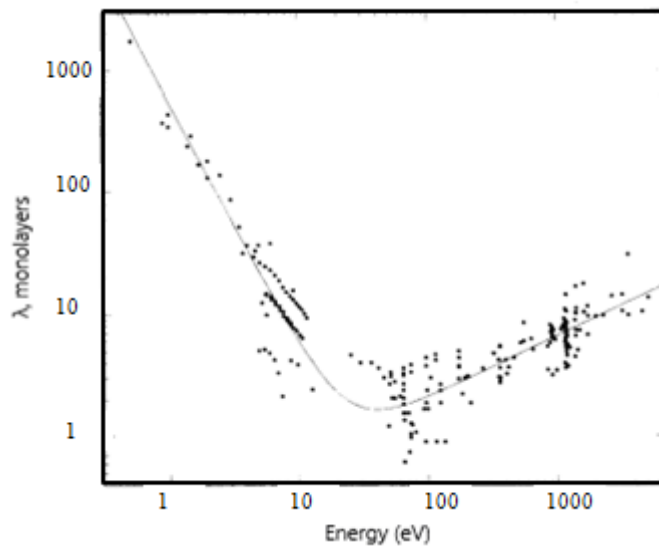


Figure 14: Curve showing the dependence of λ from the kinetic energy (eV), Compilation by *Seah* and *Dench*, adapted from [59]

The inelastic mean free path λ is the average distance an electron can travel without collision and losing part or all of its energy due to inelastic collision. *Seah* and *Dench* made a compilation of measurements of λ in dependence of kinetic energy. In Figure 14 λ is depicted as monolayers. Typical energy in XPS ranges from 250-1500 eV, which corresponds to 4-8 monolayers. Photoelectrons, which can escape into the vacuum and are detected, therefore have to originate at or very close to the surface [58].

The fundamental parts of an XPS-instrument are -an X-ray source, extraction optics, energy filters, a detection system and a vacuum pump [58]. The XPS-analysis of this work was done with the help of a SPECS XPS-spectrometer equipped with a monochromatic Al- K_{α} X-ray source (μ Focus 350) and a hemispherical WAL-150 analyzer. The aim was to use this method of analysis to determine the chemical composition and assess the bonding environments of the wear tracks.

3.8 Viscometer

As already mentioned in chapter 2.1 Friction, viscosity is also referred to as internal friction. The more viscous a fluid is, the stronger the particles are bound to each other.

If one imagines 2 plates separated by a liquid adhering to both plates, one can prove experimentally that the force to move a plate is proportional to the area and speed of the plate, but antiproportional to the distance between the two plates. By adding a proportionality constant η , the dynamic viscosity, the following equation is obtained:

$$F = \eta \cdot \frac{A \cdot v}{x} \quad (3)$$

F = Force (N)

A = surface area of plate (m²)

v = speed of plate (m/s)

x = distance between plates (m)

η = dynamic viscosity (Ns/m²)

A substance therefore has a viscosity of 1 Ns/m² if, with a plate size of 1 m² and a distance between the plates of 1 m, a force of 1 N is required to displace the plates against each other at a speed of 1 m/s. The force of 1 N is used to displace the plates against each other at a speed of 1 m/s. The force of 1 Ns/m² is used to displace the plates against each other at a speed of 1 m/s. If η is independent of the speed, it is called Newtonian fluid. The ratio of dynamic viscosity η to density ρ is further referred to as kinematic viscosity μ [60].

Viscometers are instruments for measuring the viscosity of fluids. There are many different versions and designs of viscometers. One family is formed by rotation viscometers that work according to the idea that the required torque to rotate an object in a fluid is a function of the viscosity of that fluid. This torque is measured at known speed.

A special form of a rotation viscometer is the Stabinger Viscometer, which was used in this work and is able to determine the dynamic viscosity and density of liquids and also can calculate the kinematic viscosity according to ASTM D 7042. The measuring cell contains a tube rotating at a constant speed, which is filled with the liquid sample; the measuring rotor floats in it. The viscosity is calculated from an eddy current torque measurement; the density measurement is carried out according to the oscillating U-tube principle [61].

4 Results & Discussion

The experiments were performed in a ball-on-disc setup (Figure 11) with reciprocating oscillation. The Ball, which had a diameter of 10 mm and the disc were made of 100Cr6 steel, a standard alloy with the material number 1.3505. Table 5 provides the composition of the alloy.

Table 5: Chemical composition of 100Cr6 steel in wt% [62]

C	Cr	Si	Mn	P	S	Mo
0.93-1.05	1.35-1.6	0.15-0.35	0.25-0.45	0.025	0.015	0.10

The standardized SRV discs were ground up to mesh size 4000, cleaned with isopropanol in an ultrasonic bath for 10 minutes and rinsed off with distilled water. The balls were cleaned in the same way. Then the ball and disc were installed in the tribometer and the respective precursor was distributed on the surface of the disc. After the temperature constancy had been set, the experiment was carried out. At the end of the test, the disc and ball were rinsed with isopropanol/ethanol and stored in aluminum foil and sample bag until analysis. Figure 15 shows an untreated SRV disc.

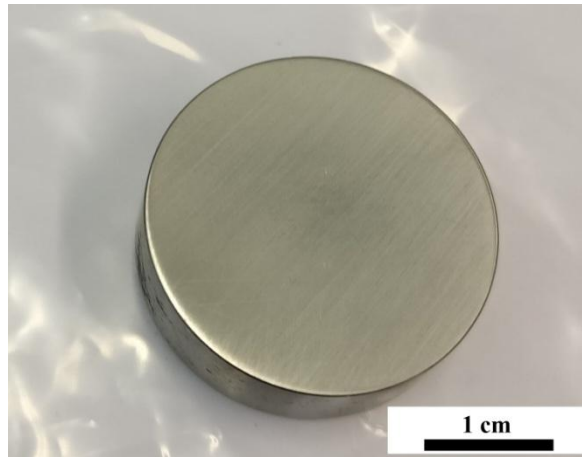


Figure 15: Untreated SRV disc

The tests were carried out at different temperatures between room temperature and 175 °C. After some preliminary tests, the following fixed parameters were found to be ideal.

Table 6: Fixed parameters for test execution

Time	Load	Frequency	Stroke
150 s	5 N	5 Hz	2 mm

In Figure 16 the two tribometers, which were used, are displayed.



Figure 16: SRV 5 tribometer located at the Austrian excellence center of tribology AC2T in Wiener Neustadt (left), and Optimol tribometer located at the technical university of Luleå (right)

4.1 No precursor

Tests were i.a. carried out without a precursor to be able to better compare the effect of lubrication. These tests were executed in the same way as described above, but without the addition of a precursor.

4.1.1 Friction analysis

The following graph shows the COF at different temperatures.

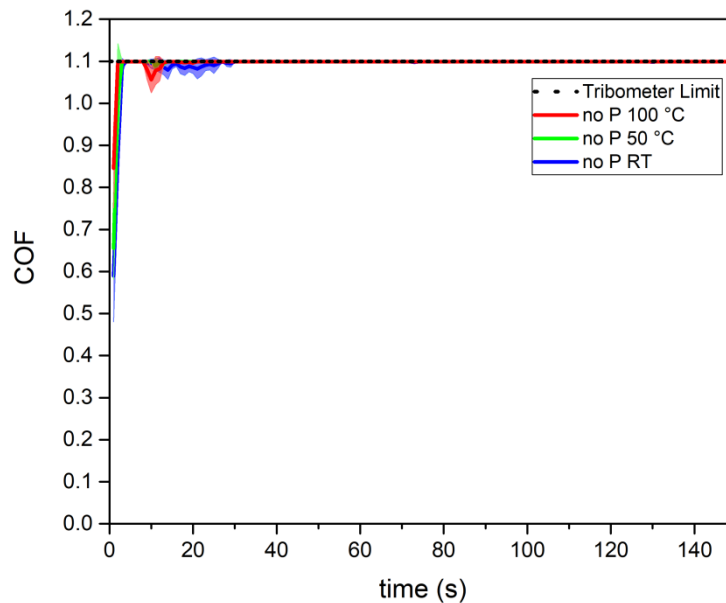


Figure 17: Coefficient of friction for no precursor at different temperatures

As shown in Figure 17, the role of temperature plays only a minor role here. The measured COF is very similar for all three temperatures studied. Starting with values between 0.5 and 0.8 it approaches 1.1 quickly within seconds after the experiment begins. Only between 10 and 40 seconds are small deviations from this value. Afterwards the COF for all 3 temperatures is constant at 1.1, which also corresponds to the recording limit of the tribometer and is represented by the dotted line. Here we are in the regime of solid friction, where high COFs are typical.

4.1.2 Wear

The following figure shows the wear rates at different temperatures.

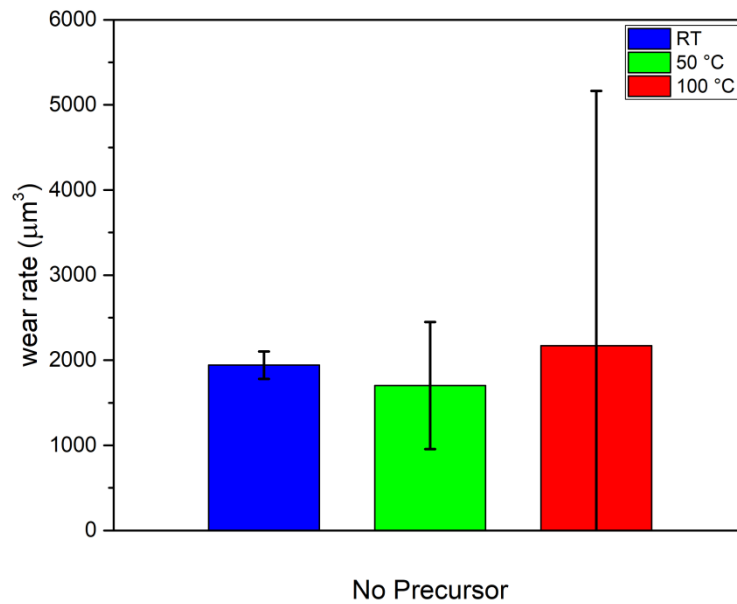


Figure 18: Wear rate for no precursor at different temperatures

As it can be seen in Figure 18, the temperature only plays a minor role in the wear rate. At all 3 temperatures the average rate is about the same. The main difference is, however, that the standard deviation increases with higher temperature. At 100 °C, it is even so large that the entire bar is afflicted with uncertainty. This might be due to the measurement routine of the wear volume and also because of the inhomogeneity of the wear tracks.

4.1.3 SEM & EDS analysis

The following figure shows images of a wear track at 100 °C.

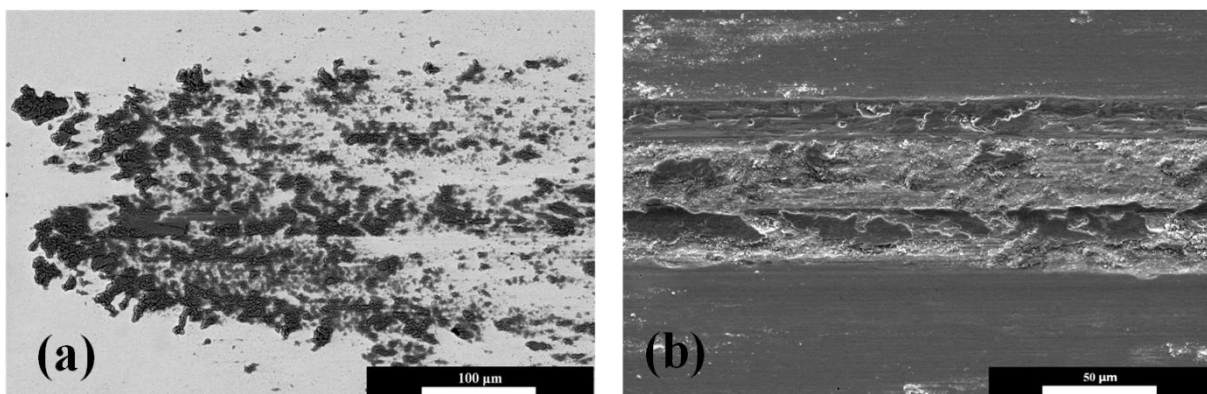


Figure 19: SEM images of a wear track at 100 °C, (a) BSE image at the edge of the wear track, (b) SE image in the middle of the wear track.

Image (a) was generated by backscattered electrons, which are sensitive to atomic numbers. Since dark areas indicate lighter elements and in this experiment only steel was

rubbed against steel, there is a high probability that these are corroded oxidic areas. Image (b), which was generated using secondary electrons, shows the topographical course within the wear track quite clearly. Both pictures also illustrate the prevailing wear mechanism. The flaky structure of the track suggests adhesive wear. The increased temperature, friction and pressure lead to welds between disc and ball, which rupture again and result in the said structure.

EDS analysis was also carried out on this sample at 100 °C, primarily to confirm the suspicion of oxidic components in the dark areas of the wear track.

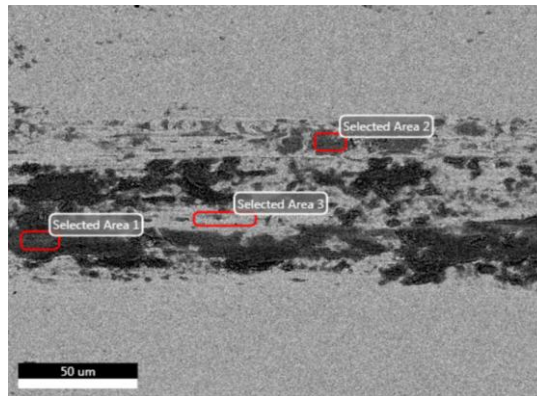


Figure 20: SEM image including the selected areas for the EDS analysis. Visible is the wear track of a sample at 100 °C

Figure 20 shows the selected areas where an ADS analysis was performed. Area 1 is in the darkest zone, whereas area 2 is in a lighter grayish region and area 3 is in a very bright region. The proportions of Fe, O, C and Si were measured. As expected, the O portion is highest in area 1 and lowest in area 3. The assumption of oxidic components in the dark areas is therefore permissible. Minimum values of Si were measured in all 3 areas. However, this is probably due either to detector-conditioned artificial peaks or to the small components of Si in the steel.

4.2 Precursor 1

4.2.1 Friction analysis

The following figure shows the course of the COF for different temperatures and the temperature dependence of the viscosity of the tested precursor.

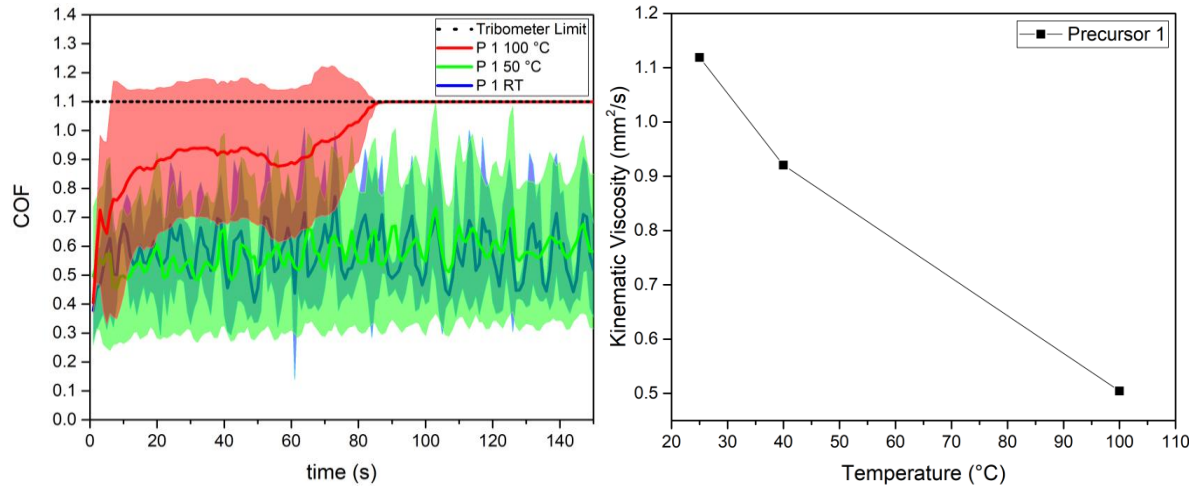


Figure 21: Coefficient of friction for precursor 1 at different temperatures (left) and the dependence of the kinematic viscosity on the temperature (right)

As shown in Figure 21, the COF for room temperature and 50 °C is very similar. The curve of the COF fluctuates and has a very large standard deviation, which is represented by the shaded areas. At 100 °C, the COF value starts at about 0.4, similar to RT and 50 °C, and then rises to about 0.9 within 20 s. After another 50 s, the COF approaches the value 1.1. There is in principle also a very high standard deviation; however the mean value between 20 and 70 s is quite constant. It has also to be mentioned that the precursor already began to evaporate at this temperature. This explains the increase of the COF and the final convergence to 1.1, the limit of the tribometer. As can be seen in the graph on the right, the viscosity of the precursor also decreases with increasing temperature, as expected. It is reduced by about half between room temperature and 100 °C and is therefore certainly also a reason for the change in COF, although probably a smaller one than the evaporation effect.

4.2.2 Wear

The wear rates of precursor 1 are shown in Figure 22.

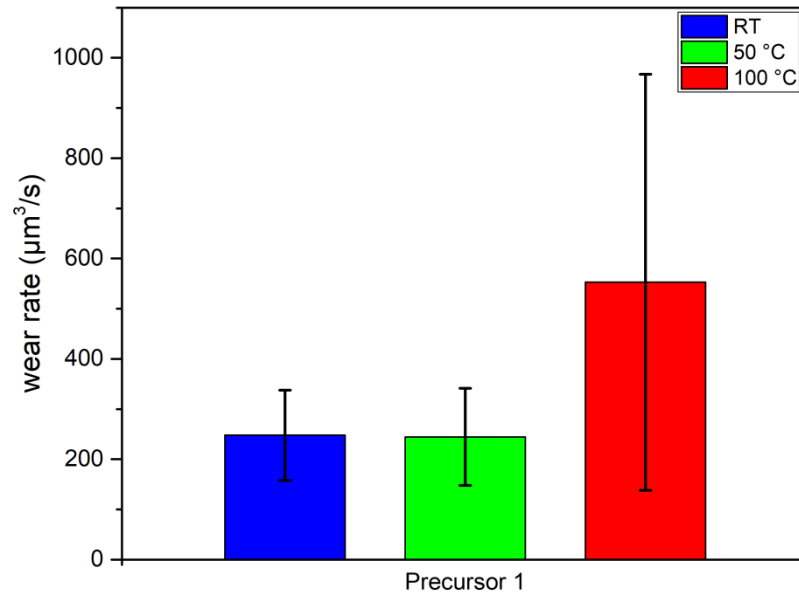
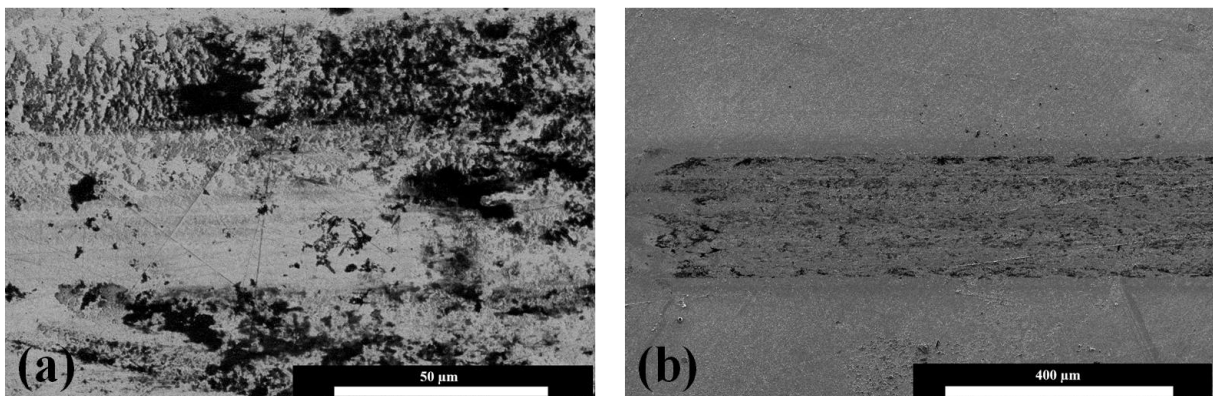


Figure 22: Wear rate for precursor 1 at different temperatures

If the determined wear rates are compared with the COFs in Figure 21, a good correlation can be seen. For room temperature and 50 °C, the rate including the standard deviation is approximately identical. As expected, at 100 °C this rate is significantly higher. The high standard deviation is striking here. Since, as mentioned above, the precursor already evaporates at these temperatures, it is reasonable to assume that in some experiments too little lubrication was present and therefore the friction increased. Evaporation of the precursor made it difficult to repeat the experiments under the same conditions.

4.2.3 SEM & EDS analysis

The following figure shows SEM records of the wear track for precursor 1.



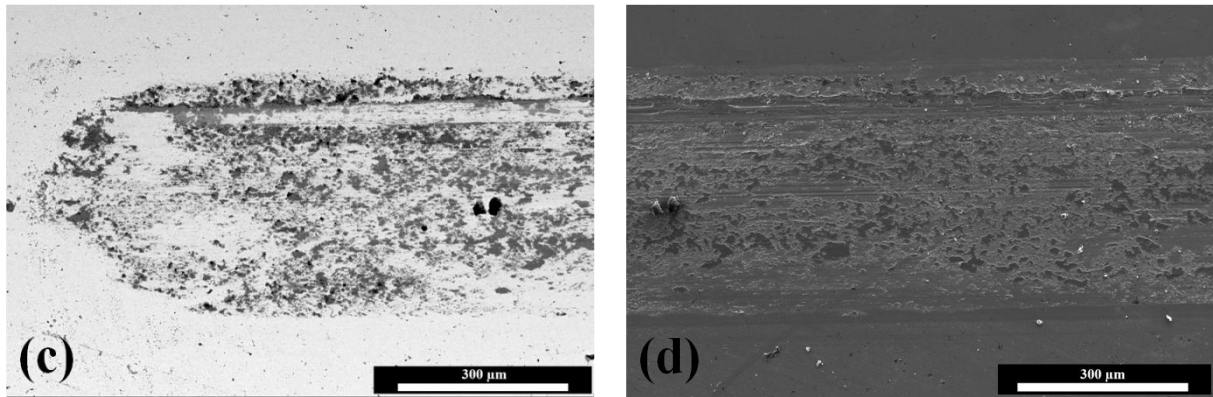


Figure 23: SEM images of a wear track, (a) BSE image of the track at RT at the edge, SE image of the track at RT, (c) BSE image of the track at the edge at 100 °C and (d) SE image of the track at 100 °C

Image (a) was generated by backscattered electrons and gives an overview of the element distribution within the wear track. The same is true for figure (c). The difference between these two images is that the spots in image (a) are clearly darker than in image (c). As mentioned above, the precursor already evaporated at 100 °C, so it is reasonable to assume that the dark spots in figure (c) represent corroded areas or solid reaction layers of substrate and precursor. In figure (a), the dark or black areas could be residues of the precursor that have partially or not yet reacted with the substrate. If one now compares image (b) with image (d), the adhesive wear mechanism, which can be recognized by the flaky structure, can be seen much better at (d). This can also be explained by the evaporation of the precursor and thus similar conditions as in the experiments without precursor (Figure 19).

EDS analyses for samples at RT and 100 °C were also performed.

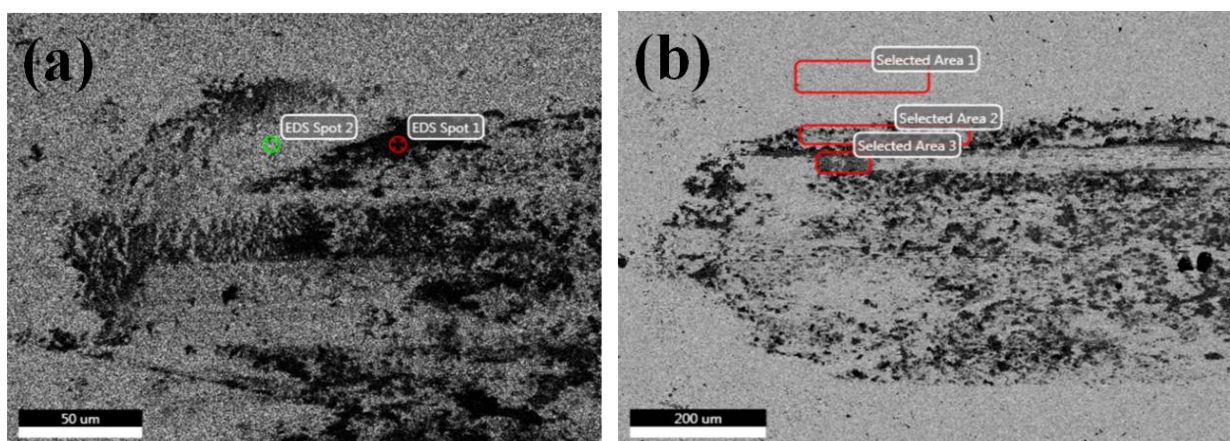


Figure 24: SEM image including the selected areas for the EDS analysis. Visible is the wear track of a sample at RT (a) and at 100 °C (b)

Figure 24 on the left shows the SEM image of the sample at RT (a). In summary the EDS analysis for spot 1 showed very high O values, but also C, N and Si were present in large quantities. Spot 2, on the other hand, is largely composed of Fe and smaller proportions of O

and C. The EDS analysis for spot 1 showed very high O values, but also C, N and Si were present in large quantities. It is therefore reasonable to assume that in the dark spot 1 mostly residues of the precursor were measured and in spot 2 mainly the partially corroded surface of the steel disc was measured. Figure (b) reveals a result similar to that obtained by analyzing the samples without precursors. Area 1, which is outside the wear track, shows the composition of the 100Cr6 steel. Areas 2 and 3 have much higher O contents. Si was only measured in very small quantities.

4.2.4 Raman analysis

The following figure shows the Raman spectra of precursor 1 at RT and the corresponding wear track with marked measuring points.

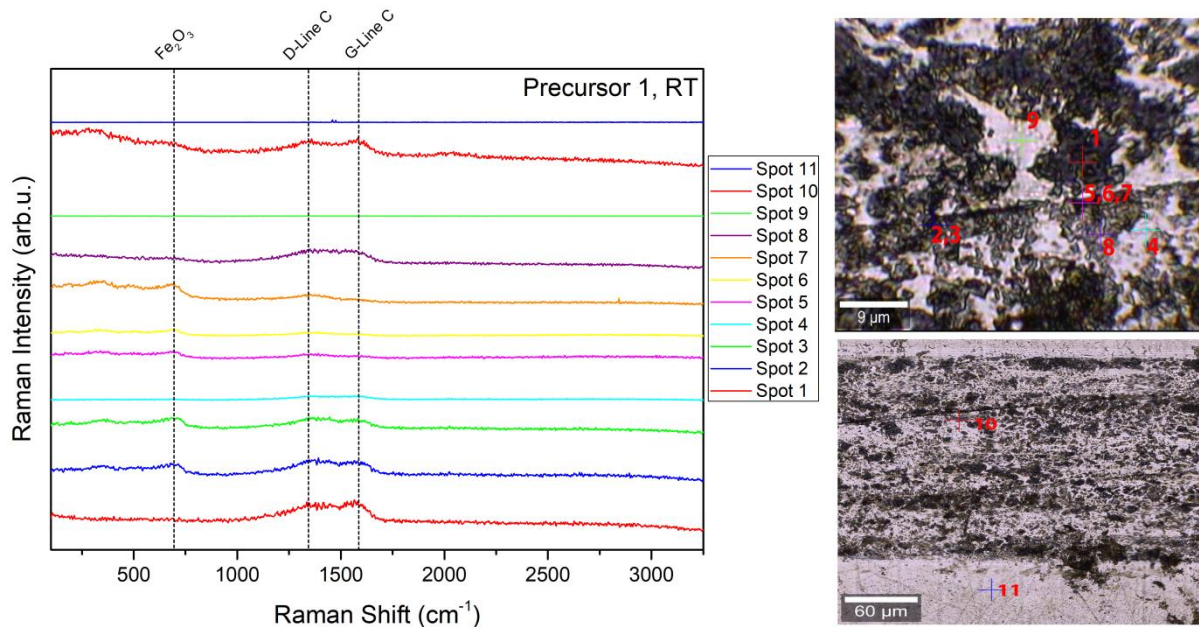


Figure 25: Raman spectra for precursor 1 at RT at different positions in and off the wear track

On the left side of Figure 25 the raman spectra of each of the 11 measuring spots can be found, the right side shows images with information on where the measurements were taken on and adjacent to the wear track. Spots 1-10 were all measured on the wear track, spot 11 however beside it. Spot 11 can therefore be used as a reference. There are no peaks in the spectrum for this spot. The only peaks worth mentioning concerning spots 1-10 are at approximately 710 cm^{-1} , 1350 cm^{-1} and 1580 cm^{-1} . The bands at 1350 cm^{-1} and 1580 cm^{-1} can be assigned reliably. They should correspond to the D- and G-band of carbon, where the D-band is disorder induced and the G-band is formed by in plane bond stretching of the sp^2 carbon. These two bands are described in numerous publications in connection with silicon carbonitride (SiCN) [63, 64] and silicon carboxide (SiOC) [65, 66]. The band at 710 cm^{-1} is

most likely a phase of iron oxide. There are many different phases that can be considered [67]. Since the unambiguous assignment is not necessary here, the assumption of a type of iron oxide is satisfactory.

The following figure shows the Raman spectra of precursor 1 at 100 °C and the corresponding wear track with marked measuring points.

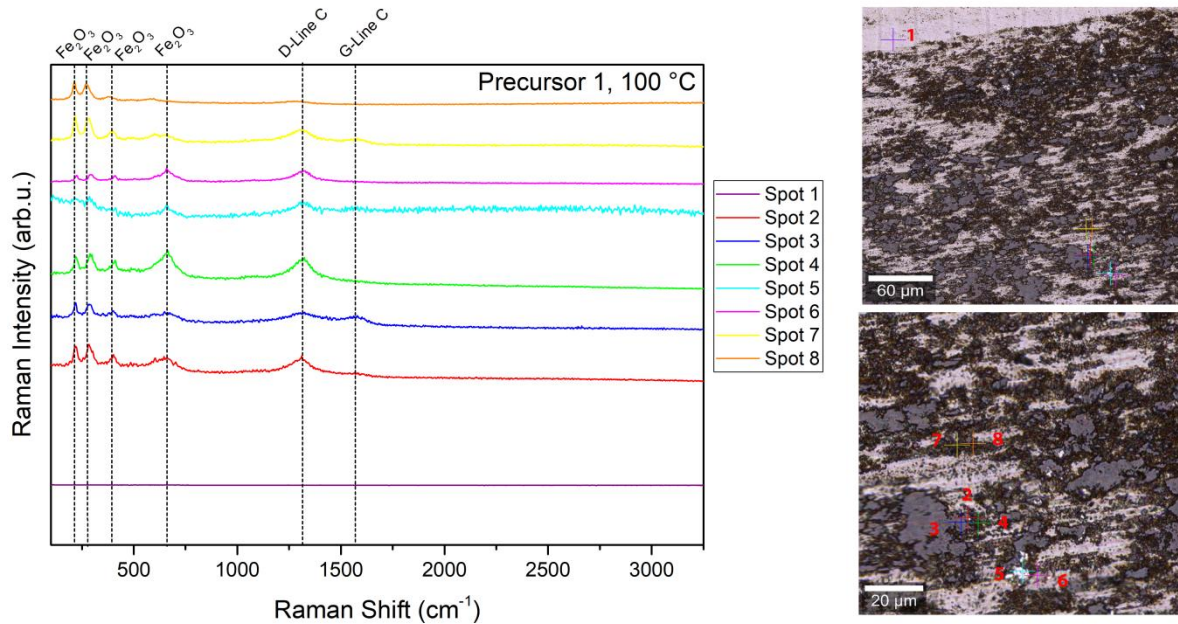


Figure 26: Raman spectra for precursor 1 at 100 °C at different positions in and off the wear track

Figure 26 also shows on the left side the Raman spectra of the different measuring spots and on the right side the corresponding images with the wear track where the measuring spots are marked. With the exception of spot 1, all other spots 2-8 are within the wear track. Here, too, the D- and G-band of the carbon can be found at about 1320 cm^{-1} and 1580 cm^{-1} respectively. As already mentioned above, these bands could be indications for possible SiCN, or SiOC formations. Otherwise there are still raman peaks at about 220 cm^{-1} , 290 cm^{-1} , 410 cm^{-1} and 660 cm^{-1} , that can be assigned to different iron oxides [67].

4.2.5 TEM analysis

The following figure shows a TEM image of a foil prepared with FIB from the wear track of a specimen with precursor 1 at 100 °C.

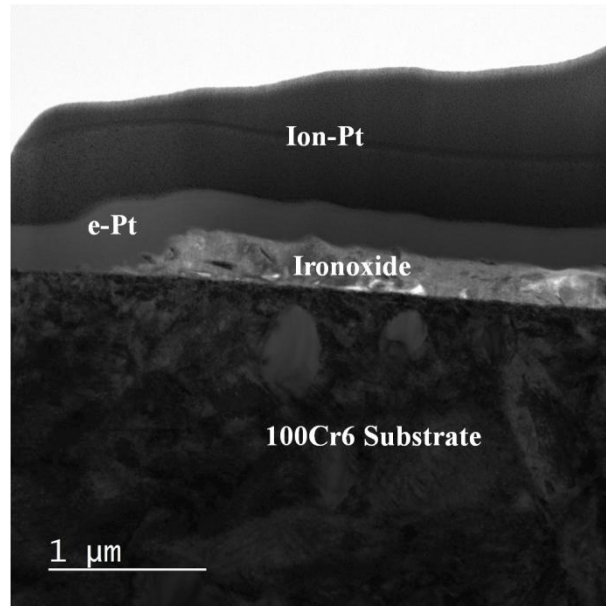


Figure 27: TEM image of a foil from the wear track of precursor 1 at 100 °C

The section of the prepared TEM film shown in Figure 27 shows the layered structure. At the bottom is the pristine steel substrate, the next layer consists of iron oxide formed by tribocorrosion and at the top is the protective platinum layer applied in the run of the sample preparation by FIB.

4.3 Precursor 2

4.3.1 Friction analysis

Figure 28 depicts the course of the COF of precursor 2 at the chosen temperatures and the dependence of the respective viscosity from the temperature.

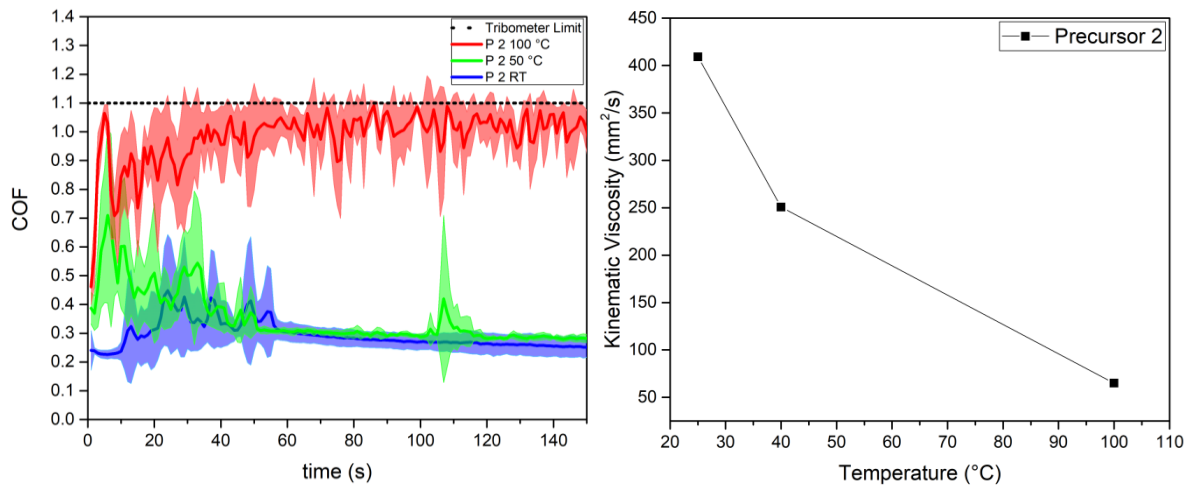


Figure 28: Coefficient of friction of precursor 2 at different temperatures (left) and the dependence of the kinematic viscosity on the temperature (right)

For room temperature and 50 °C the development of the COF is very similar. At the beginning of the experiment, the values fluctuate relatively strongly and begin to stabilize after about 60 s with a short exception (at about 110 s). A constant COF after initial fluctuation could indicate a possibly formed tribofilm. At 100 °C, the COF is significantly greater. The entire recording at this temperature is characterized by unstable, high COF values close to the tribometer limit. A look at the temperature dependence of the precursor's viscosity reveals that it has been reduced to about one eighth between room temperature and 100 °C. This effect is likely to contribute to the considerable increase in COF.

4.3.2 Wear

The following figure represents the wear rates of precursor 2.

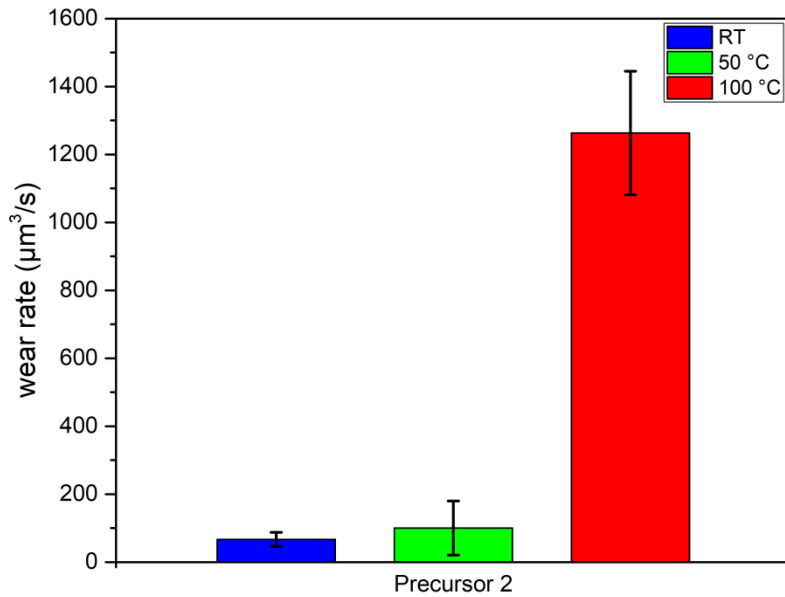


Figure 29: Wear rate for precursor 2 at different temperatures

Figure 29 correlates well with Figure 28 as far as the experiments at room temperature and 50 °C are concerned. Low COFs result in low wear rates. The rate at 50 °C is slightly higher than at room temperature, but due to the larger standard deviation this is not very meaningful. The wear rate at 100 °C is remarkable, which is many times higher than that at lower temperatures. With precursor 1, an attempt was made to explain this by means of evaporation processes. With precursor 2, however, this was definitely not the case. Rather, the decreasing viscosity could be a reason for this development.

4.3.3 SEM & EDS analysis

The following figure shows SEM pictures of the wear track at 100 °C.

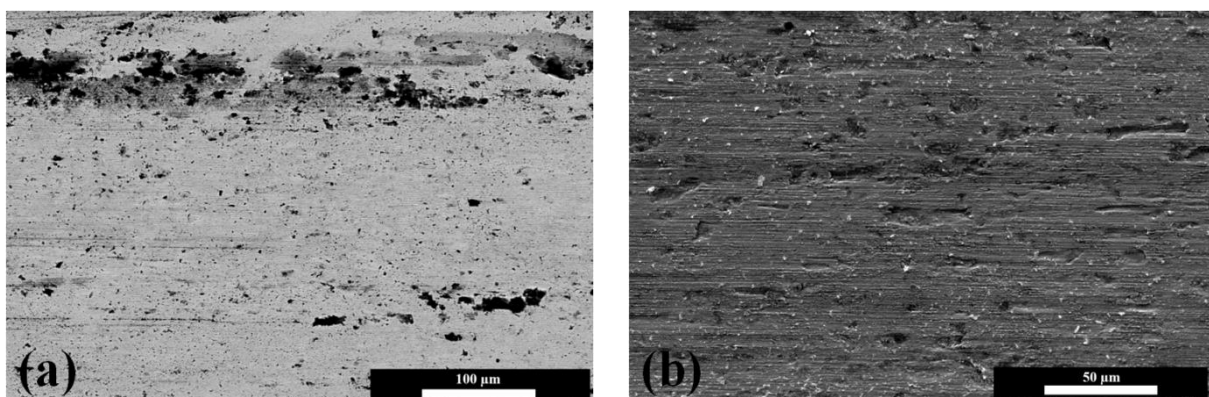


Figure 30: SEM images of a wear track, (a) BSE image in the middle of the track at 100 °C, (b) SE image in the middle of the track at 100 °C

Since image (a) was generated by backscattered electrons, it contains little to no topographic information. The dark areas in the wear track indicate residues of the organic precursor that may have reacted with the substrate. The secondary electrons image (b) shows

the extent of wear. The sample is streaked with scratches and craters from which sample material has been broken out.

The EDS analysis of this sample gives first indications of the chemical composition of the wear track.

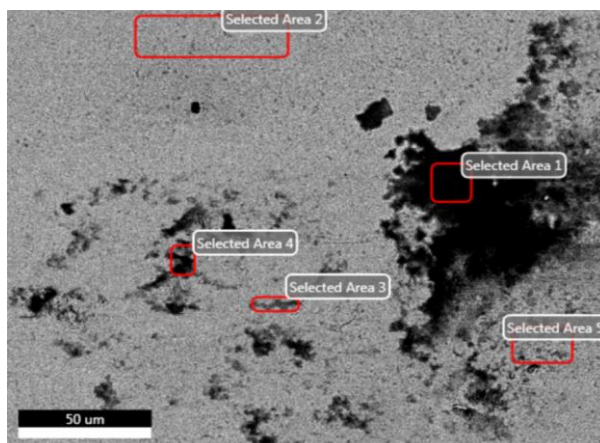


Figure 31: SEM image including the selected areas for the EDS analysis. Visible is the edge of the wear track of a sample at 100 °C

The EDS analysis of the areas in Figure 31 has shown that the dark areas 1, 3 and 4 have high C contents, but O and Si are also present in large quantities. The brighter areas 2 and 5 are dominated by Fe. However, smaller amounts of C and O as well as Si can also be measured here.

4.3.4 Raman analysis

The following figure shows the Raman spectra of precursor 2 at RT and the corresponding wear track with marked measuring points.

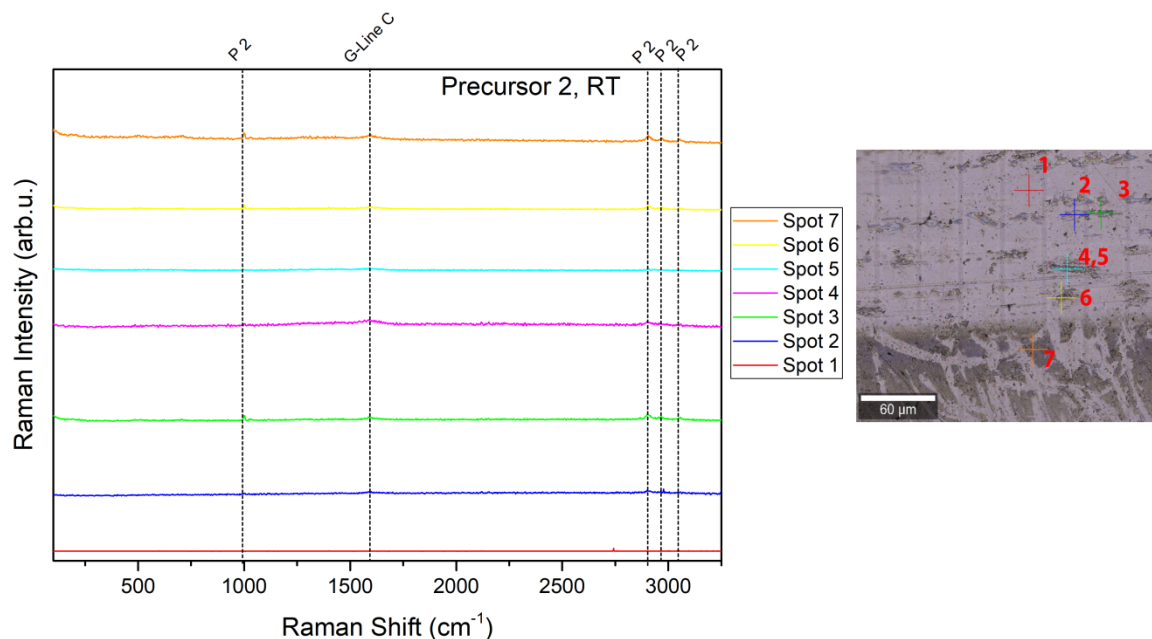


Figure 32: Raman spectra for precursor 2 at RT at different positions in and off the wear track

In contrast to precursor 1, no D-band of carbon can be found in Figure 32 for precursor 2 at RT. However, the G-band is found again at about 1580 cm^{-1} . In general, the signals for this sample are very weak. It is interesting to note that spot 7, which is the only spot next to the wear track, has the same bands as the other spots on the wear track. The other bands are at about 1000 cm^{-1} , 2905 cm^{-1} , 2970 cm^{-1} and 3050 cm^{-1} and were assigned to the precursor after comparison with its Raman spectrum. So these are probably unreacted precursor residuals [68].

The following figure shows the Raman spectra of precursor 2 at $100\text{ }^{\circ}\text{C}$ and the corresponding wear track with marked measuring points.

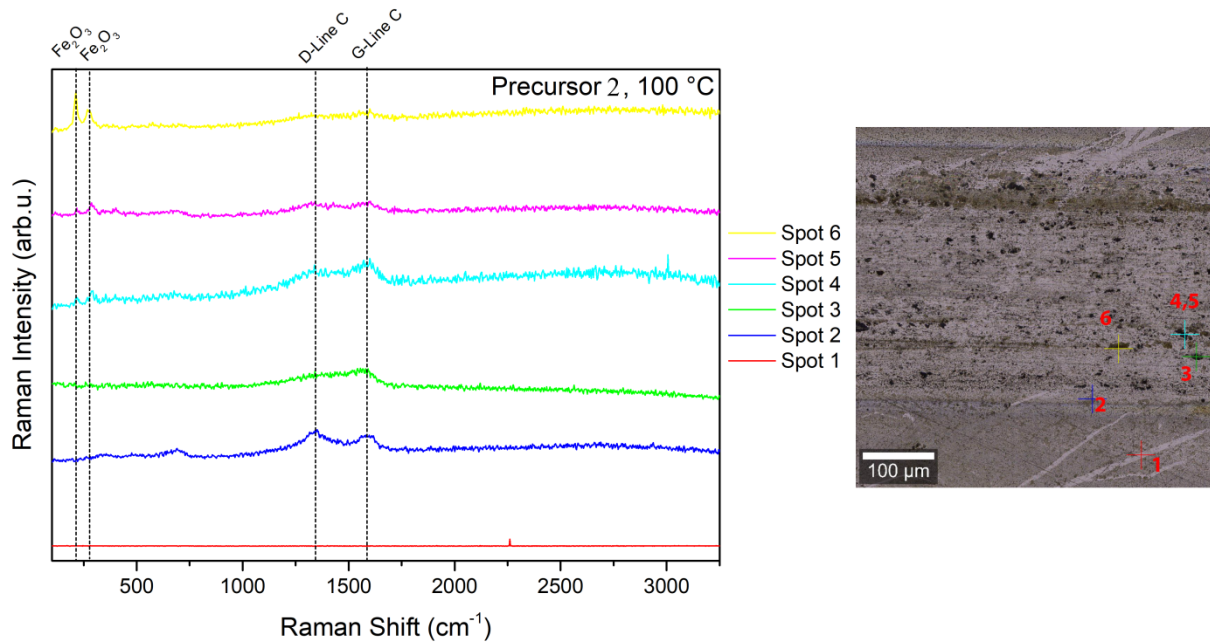


Figure 33: Raman spectra for precursor 2 at 100 °C at different positions in and off the wear track

In Figure 33, when looking at the Raman spectra on the left side, one can again find both bands of carbon, the D-band at about 1350 cm^{-1} and the G-band at about 1580 cm^{-1} , which indicate the possible formation of SiOC or SiCN. However, given the chemical composition of the precursor, the first seems more likely. This applies to the spots 2-6, which are on the wear track. Spot 1, on the other hand, which is next to the wear track, has no bands at all. In addition to the two carbon bands, there are further bands at about 210 cm^{-1} and 270 cm^{-1} , which can be assigned to the iron oxides as above [67].

4.4 Precursor 3

4.4.1 Friction analysis

Figure 34 shows the course of the COF as a function of the selected temperatures and the temperature dependence of the viscosity of the precursor 3.

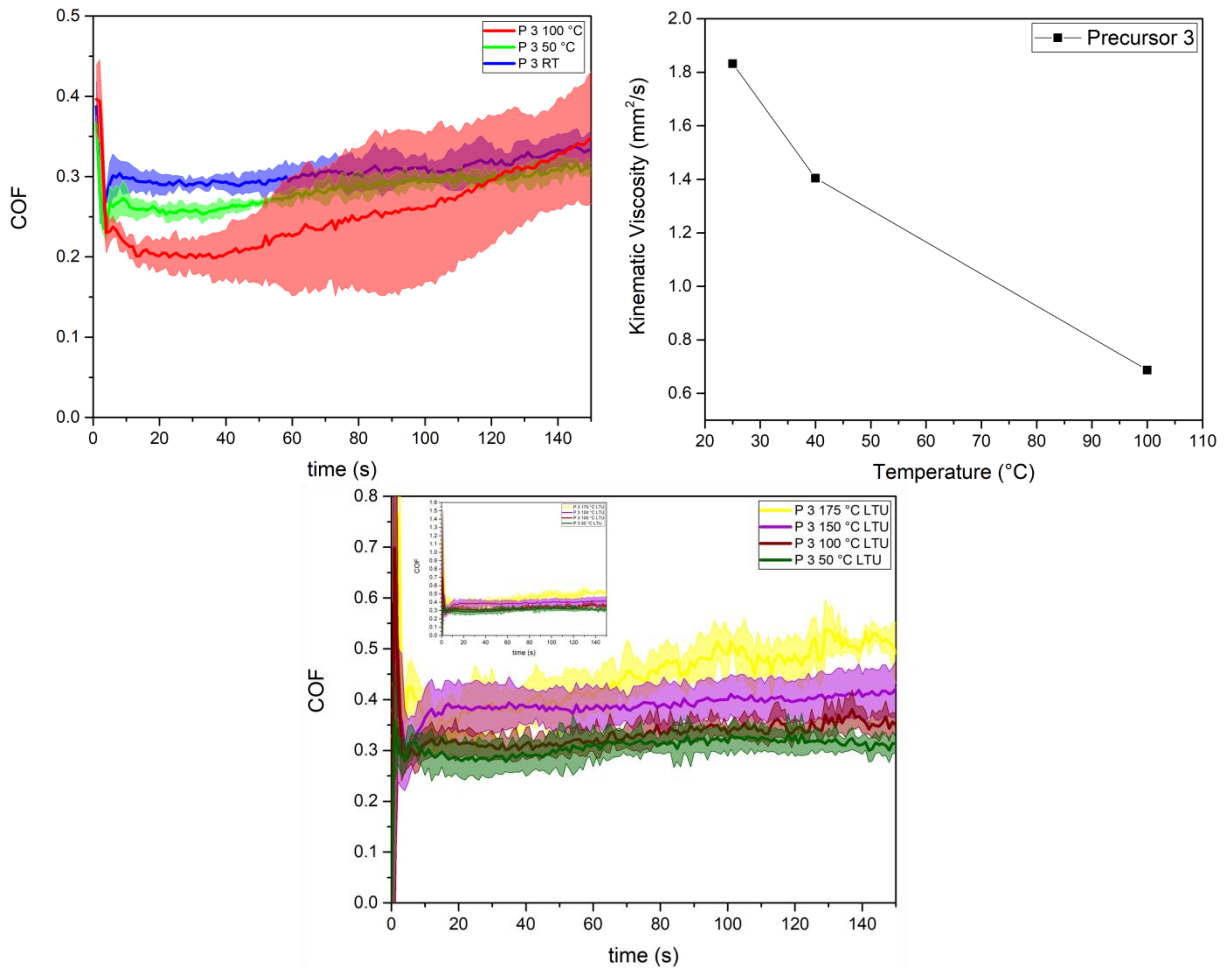


Figure 34: Coefficient of friction of precursor 3 at different temperatures (left), the dependence of the kinematic viscosity on the temperature (right) and coefficient of friction of precursor 3 at different temperatures measured at LTU (below)

As shown in Figure 34, more than 3 temperatures were investigated for precursor 3. This is primarily due to the fact that the COF dropped with increasing temperature up to 100 °C during the initial experiments (left graph). The experiments were continued in Lulea at LTU at 100 °C, 150 °C and 175 °C to see whether this behavior also applies to higher temperatures (graph below). 175 °C turned out to be the upper limit as the precursor began to evaporate at this temperature. In the legend, these experiments are marked with the addition LTU. The minimized graph at the top left has the same data as the large graph, only a different scale. It is supposed to be made clear that the tribometer limit at LTU was higher than 1.1 and thus

higher COFs could be measured. These very high values were measured at the beginning of the experiments at LTU, but the COFs decreased very quickly.

As just mentioned, the COF dropped from about 0.3 to 0.2 between RT and 100 °C. During the run of the experiment, however, the curve at 100 °C approaches the curves at 50 °C and 100 °C again. Considering that (as can be seen on the right) the viscosity is reduced to about one third in this temperature interval, this development is extraordinary. A similar result was reported in the publication by *Gonzalez Rodriguez et al.* [5] in which the same chemical compound in the form of a polymer was used. The suspicion that a tribofilm might have been formed during the experiment in a reaction between the substrate and the precursor is therefore justified. Even though the curve measured at LTU for 100 °C at the beginning of the experiment does not fully coincide with the one measured before, they approach each other to the end. At 150 °C, the COF increases again slightly, but the standard deviation is not particularly large. At 175 °C the fluctuation is greater. However, this is not least due to the evaporation of the precursor.

Since precursor 3 turned out to be the most interesting and promising with regard to a possible tribofilm, an attempt was made to find the optimal temperature to better characterize the tribofilm. A temperature as high as possible was sought, at which the COF does not show large fluctuations. The following figure shows the sequence of the experiment used to determine the optimum temperature and the resulting friction tests.

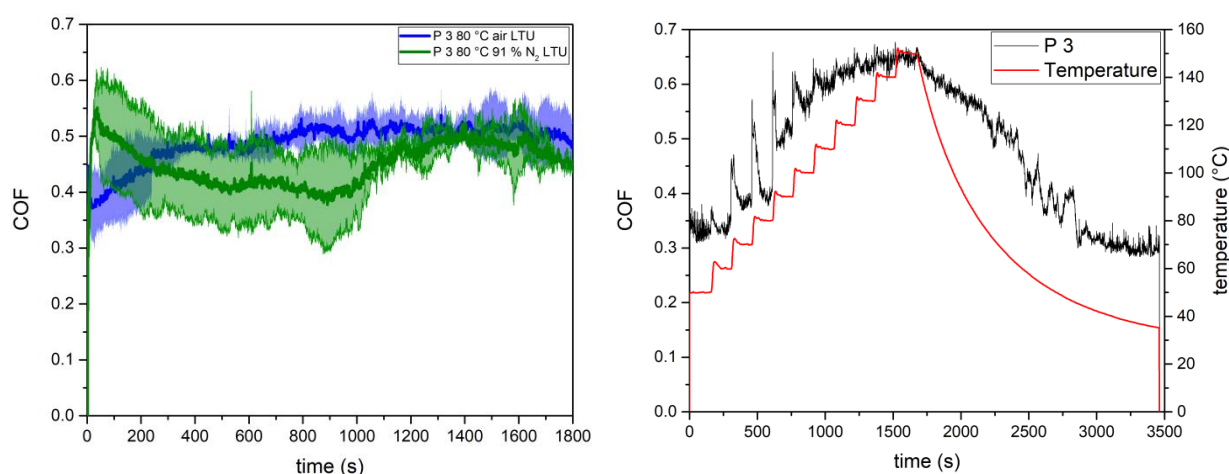


Figure 35: COF of precursor 3 at 80 °C under air and elevated N₂ atmosphere (left) and COF of precursor 3 at stepwise elevated temperatures (right)

The graph on the right of Figure 35 shows how the optimal temperature was determined for Precursor 3. Starting at 50 °C, the temperature was gradually increased by 10 °C to 150 °C every 150 s, cooled to room temperature and the COF measured. After each temperature increase, the COF increased more or less strongly at the beginning and stabilized after a few

seconds. At 90 °C the COF increased relatively strongly and for the first time also showed quite large fluctuations. Therefore, a temperature of 80 °C was found to be optimal.

The COF was then measured at 80 °C for 30 minutes. In addition, the influence of oxygen was investigated and an experiment was carried out in an elevated nitrogen atmosphere. Unfortunately, the sample chamber was not sealed enough to reach 100 % N₂, so 91 % had to be accepted. The graph of these experiments is to the left of Figure 35. The COF curve is opposite for both variants at the beginning of the measurement and approaches the end. While in normal laboratory air the friction is lower at the beginning and increases slightly, under increased nitrogen the friction is initially higher and decreases slightly. The standard deviation of the COF is significantly greater with increased nitrogen than under laboratory air. In general, however, the friction is somewhat higher than in the experiments at 50 °C and 100 °C (see Figure 34). If one considers only the first 150 s of the blue line, however, this difference is much smaller. The friction obviously increases after a longer time. It cannot be ruled out that a possible tribofilm formed will be rubbed off again after a certain time.

4.4.2 Wear

Figure 36 represents the wear rates of precursor 3 at different temperatures.

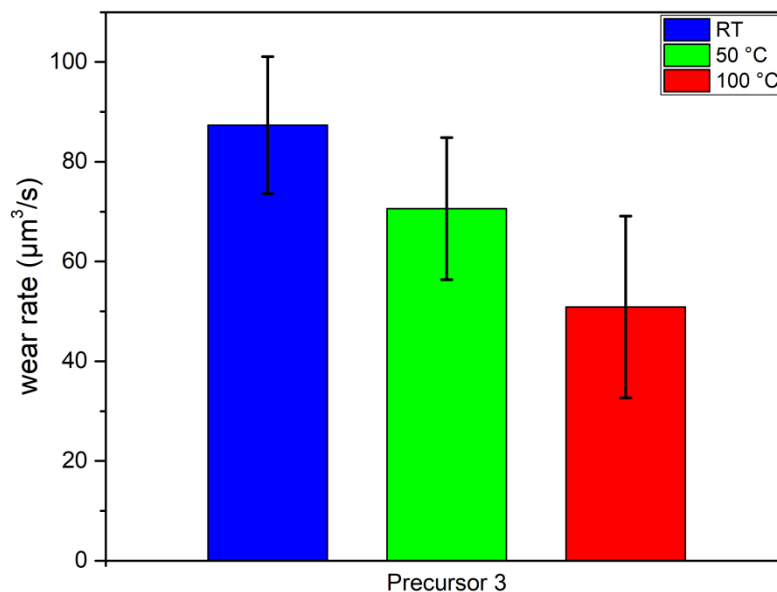


Figure 36: Wear rate for precursor 3 at different temperatures

In contrast to the other two precursors 1 and 2, precursor 3 shows a reduction in the wear rate with increasing temperature, as can be seen in Figure 36. The rates have very similar standard deviations and obviously decrease in approximately equal steps. However, a closer look reveals that the upper limit of the standard deviation at 100 °C coincides de facto with

the lower limit of the standard deviation at room temperature. It is therefore difficult to make a reliable statement here.

4.4.3 SEM & EDS analysis

The following figure shows SEM pictures of the wear tracks with precursor 3.

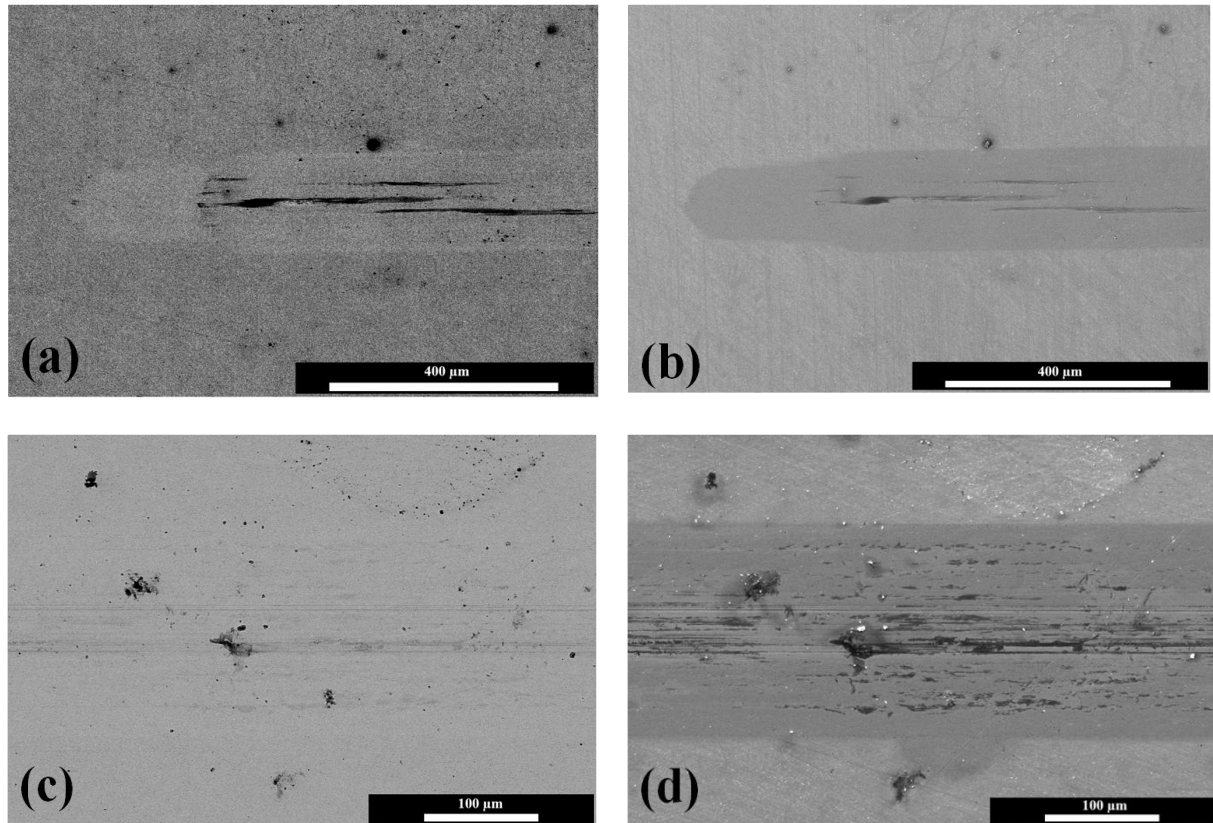


Figure 37: SEM images of a wear track, (a) BSE image at the edge of the track at RT, (b) SE image at the edge of the track at RT, (c) BSE image in the middle of the track at 100 °C, (d) SE image in the middle of the track at 100 °C

The BSE picture (a) shows the edge area of the wear track. The very fine trace is brighter than the substrate. Only a few, very fine, dark scratches can be seen. Remnants of the precursor could be found in these dark areas. Looking at the SE image (b), one gets the impression that the wear mark even has a smoother surface than the substrate. On the BSE picture (c) the wear track is almost not visible anymore. There is almost no contrast between substrate and track. The SE image (d), which represents the test at 100 °C, is very similar to the one at RT (b). Overall, the tendency of decreasing wear with increasing temperature (and Figure 36) can be seen when comparing images (a) and (c).

An EDS analysis was performed for one sample at RT and one at 100 °C.

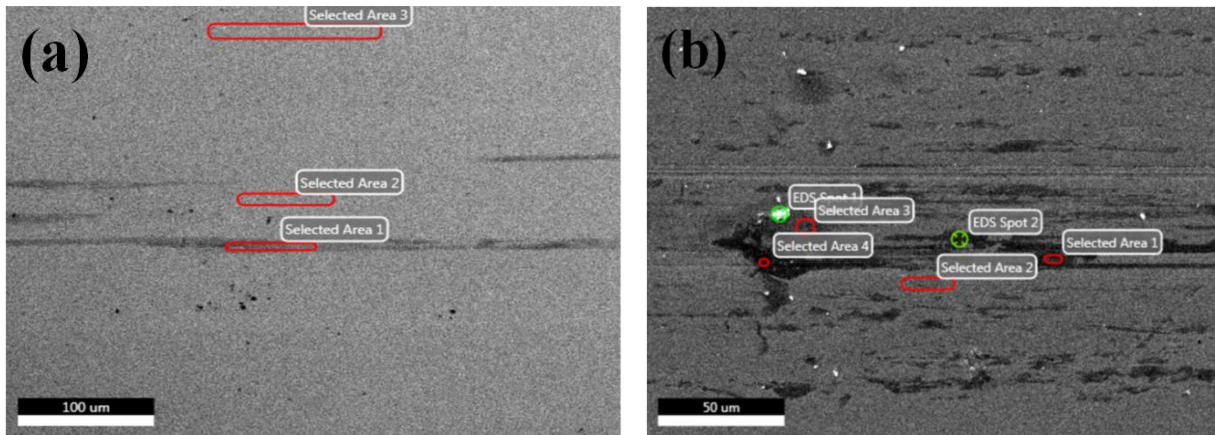


Figure 38: SEM image including the selected areas for the EDS analysis. Visible is the wear track of a sample at RT (a) and at 100 °C (b)

The left picture (a) in Figure 38 shows the 3 areas where an EDS analysis was performed. Also here the result confirms that in the dark area 1 the O content, but also the Si content is higher than in the two lighter areas 2 and 3. The right picture (b) shows the respective spots and areas for the sample at 100 °C. The left picture (a) shows the areas where the EDS analysis was performed. The tendency that in the dark areas/spots the O, C and Si content is higher than in the brighter ones is also continued here. Compared to the other two samples, the O content is significantly lower. This is also compatible with the lower COF.

4.4.4 Raman analysis

The following figure shows the Raman spectra of precursor 3 at RT and the corresponding wear track with marked measuring points.

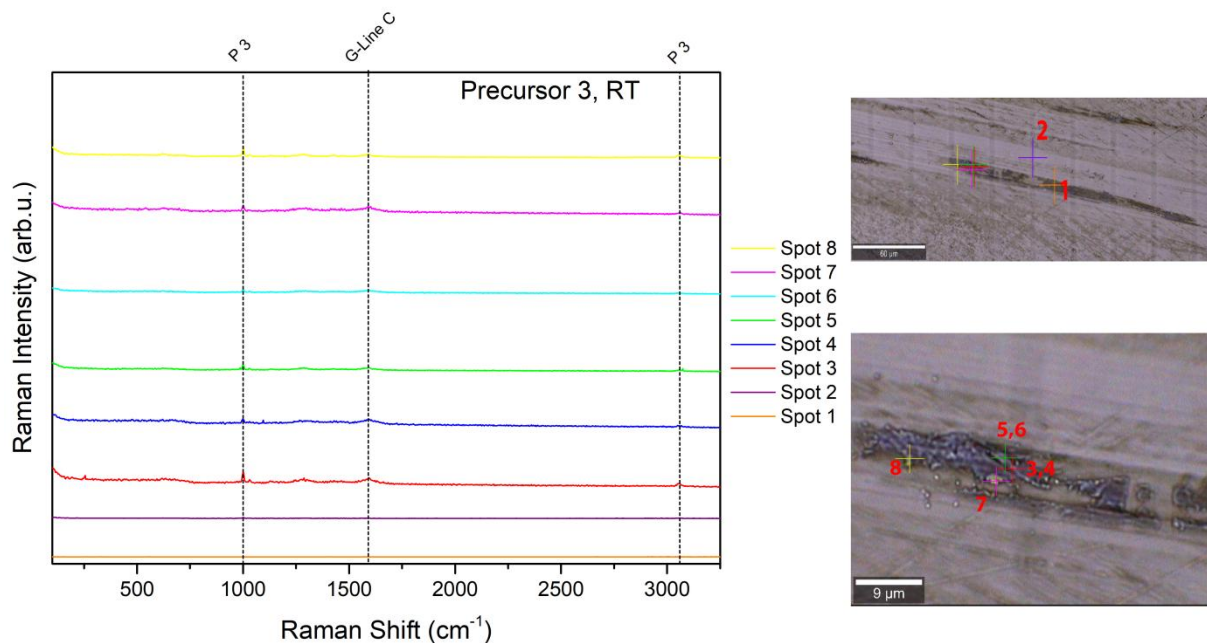


Figure 39: Raman spectra for precursor 3 at RT at different positions in and off the wear track

Figure 39 shows the Raman spectra of the measuring spots on the left side and the wear track with the marked measuring spots on the right side. The found bands are very weak. Apart from spot 2, which is located next to the wear track, the G-band of the carbon can be found at about 1580 cm^{-1} for the other measuring spots. The other two bands were somewhat more difficult to identify. Since no Raman spectrum of the precursor was available, the spectrum of triethoxyphenylsilane was compared to the spectra of Figure 39 and the other two bands at about 1000 cm^{-1} and 3060 cm^{-1} were assigned to it [69].

The following figure shows the Raman spectra of precursor 3 at $100\text{ }^{\circ}\text{C}$ and the corresponding wear track with marked measuring points.

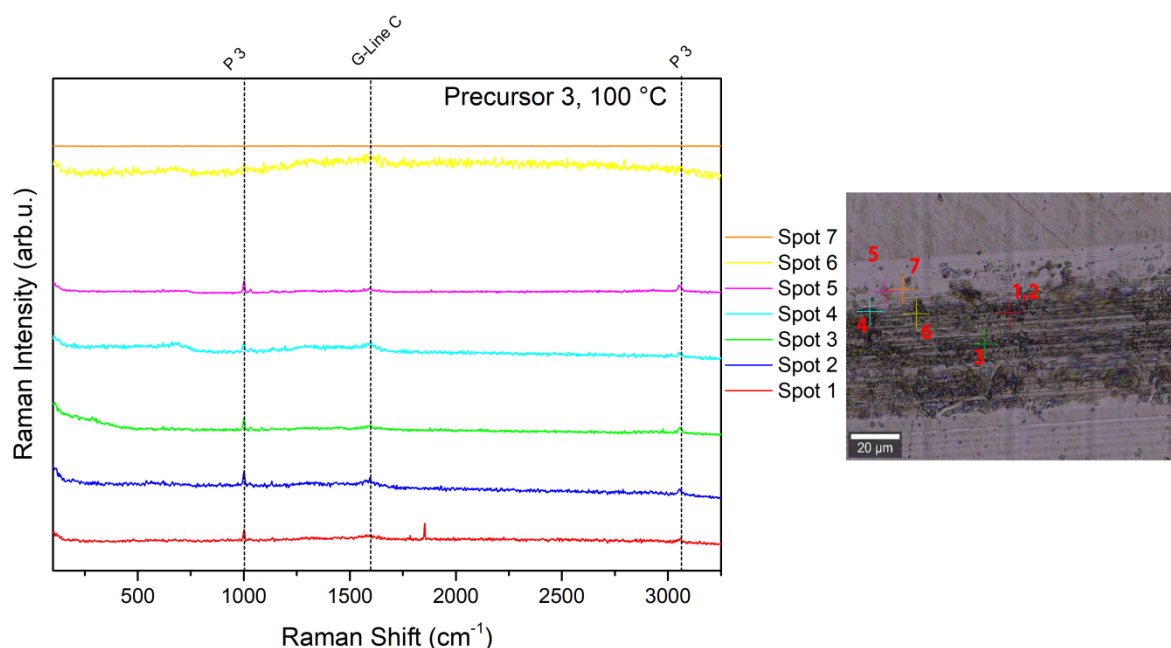


Figure 40: Raman spectra for precursor 3 at $100\text{ }^{\circ}\text{C}$ at different positions in and off the wear track

Figure 40 shows a very similar result as in Figure 39. Apart from the G-band of carbon at about 1580 cm^{-1} and the two bands at about 1000 cm^{-1} and 3060 cm^{-1} , which are assigned to the precursor as in the sample at RT, no other bands can be identified. Spot 1 is a small exception. As the only spot, it shows a relatively clear band at about 1850 cm^{-1} , which cannot be assigned after intensive research.

4.4.5 TEM analysis

The following figure shows a TEM image of a foil prepared with FIB from the wear track of a specimen with precursor 3 at $100\text{ }^{\circ}\text{C}$.

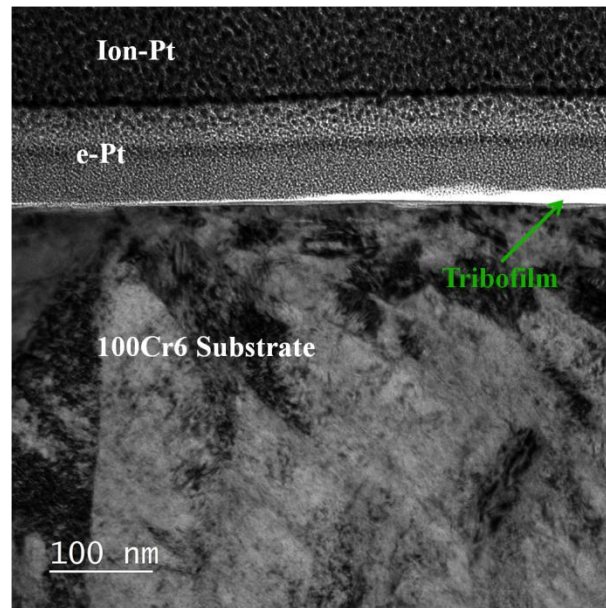


Figure 41: TEM image of a foil from the wear track of precursor 3 at 100 °C

Figure 41 shows a layered structure of the sample. The lower part consists of 100Cr6 substrate, the upper part of platinum applied by electrons and ions as protection during sample preparation. In between, a very thin, bright area can be seen. This is plausibly the formed tribofilm, which is marked in green. The thickness is not constant and it does not extend over the whole sample. Due to the extremely small thickness of a few nanometers, it is very difficult to determine the structure of this tribofilm by electron diffraction.

4.5. Comparison

In this chapter, the differences and similarities of the precursor results will be compared.

4.5.1 Friction analysis

The following figure shows the coefficients of friction of all precursors for the same temperatures in graphs.

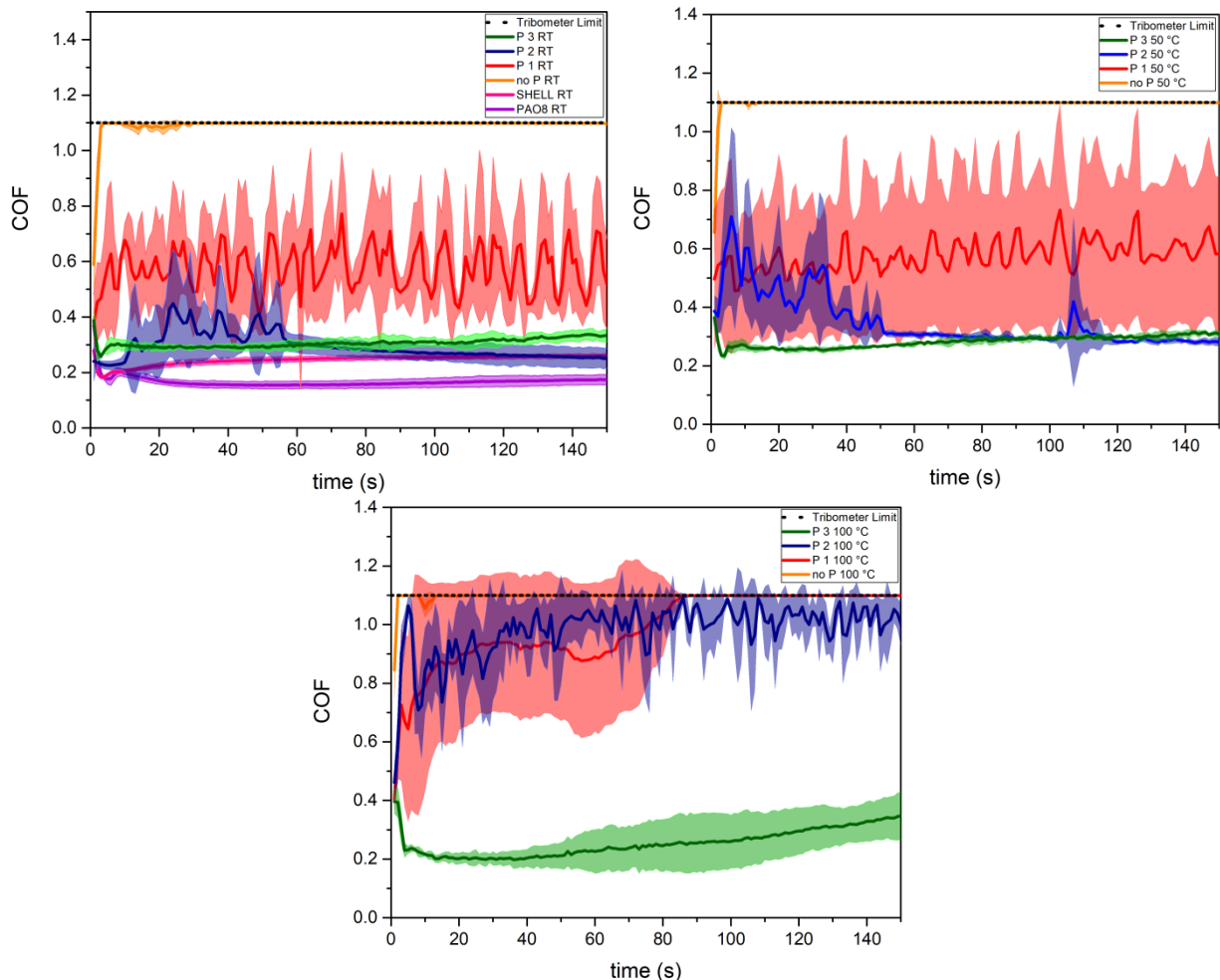


Figure 42: COF of all precursors including Shell Helix Ultra SN 0W-20 and PAO 8 at RT (top left), COF of all precursors at 50 °C (top right) and COF of all precursors at 100 °C (middle below)

Starting with the graph at top left, the COFs of two different oils have been determined in addition to the COFs of the precursors. On the one hand, Shell Helix Ultra SN 0W, engine oil, and on the other hand PAO 8 (polyalphaolefinolefin), a mineral oil without additives, were tested at RT. These two oils show an extremely stable friction behavior with minimal fluctuations. The COF values are very low for both, with PAO 8 having the lowest values. A comparison of the precursors clearly shows that the friction for precursor 1 is highest and most unstable. Precursor 3, on the other hand, shows very stable behavior, although the COF values are slightly higher than those of the two oils. Precursor 2 stabilizes after strong initial

fluctuations after about 60 s and then shows even better friction behavior than Precursor 2 and about the same COFs as SHELL's engine oil. The COF for the sample without precursor already exceeds the limit of the tribometer, which is 1.1, after a few seconds.

The graph at the top right shows a very similar result as before. Precursor 1 has the highest values of the COF and also the highest fluctuation, which has even increased compared to RT. Precursors 2 and 3 are basically very similar in the values of the COF. Also here precursor 2 needs a certain start-up time of about 50 s until the friction is stable at 110 s with a small exception. For the sample without precursor the same applies as for RT. After a few seconds the friction exceeds the limit of the tribometer.

The graph in the middle below now shows a different behavior. Precursor 1, which, as already mentioned, begins to evaporate at 100 °C, shows even higher friction values than at low temperature. After about 90 s, however, these values exceed the limit of the tribometer, presumably due to excessive evaporation. This time Precursor 2 also shows very high COFs. In contrast to the experiments at RT and 50 °C, neither the fluctuations nor the COF values decrease. Interestingly, at this temperature precursor 3 initially shows even lower friction values than at lower temperatures. The fluctuations also become greater.

4.5.2 Wear

The following figure summarizes the wear rates determined for all precursors at all temperatures.

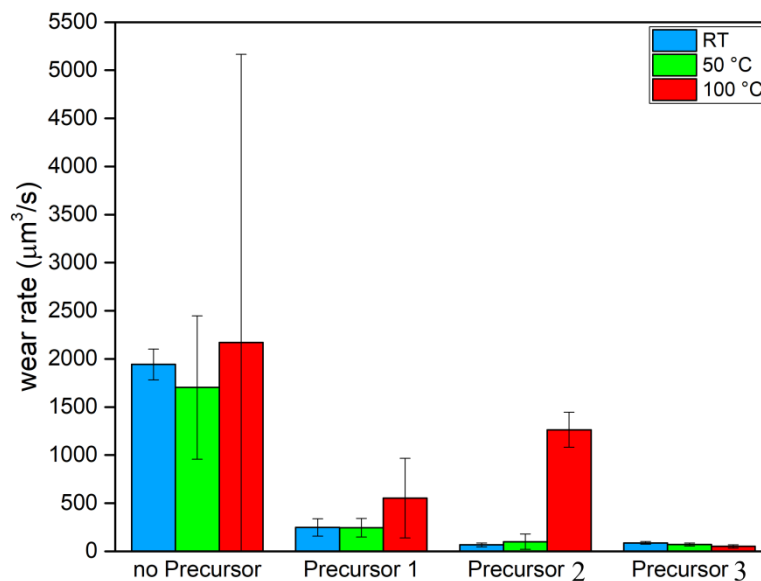


Figure 43: Wear rate for all precursors at different temperatures

The wear rates for no precursor in Figure 43 are significantly higher than those for the precursors used. The temperature obviously has no great influence on the averaged values, as there is no clear trend towards higher wear rates at higher temperatures. But what does indeed change with the temperature is the standard deviation. At RT it is very small, increases at 50 °C and extends at 100 °C over the entire bar and beyond. The tendency of rising standard deviation with rising temperature is also largely valid for the precursors tested. Precursor 1 has the highest wear rates at RT and 50 °C compared to the other two precursors. Compared to precursor 2, which shows very good wear properties at low temperatures, the rate at 100 °C does not increase as much. The development of Precursor 3, which is the only one with a low, decreasing wear rate at higher temperatures from the outset, is remarkable.

4.5.3 SEM analysis

The following figure shows a compilation of SEM images of wear marks from all precursors at 100 °C. Here the differences in wear are quite obvious.

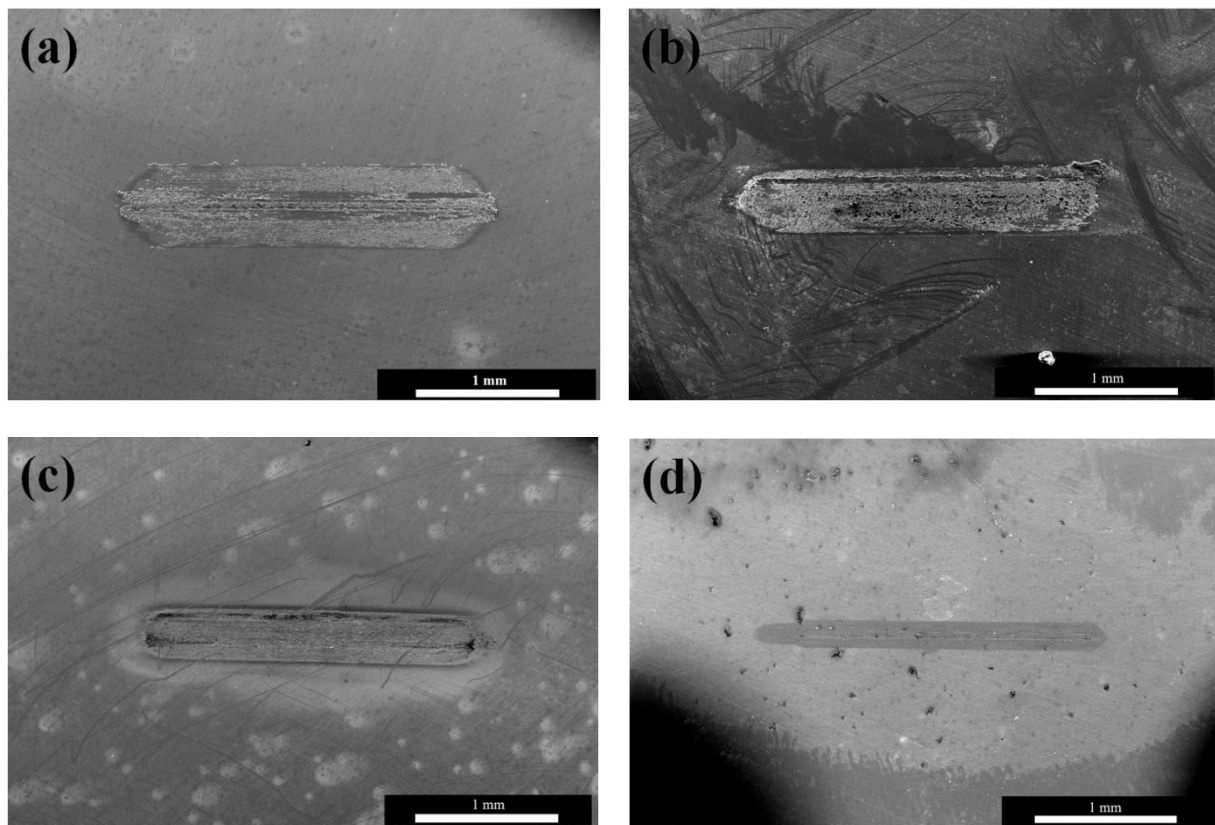


Figure 44: SE images of the wear track at 100 °C for no precursor (a), precursor 1 (b), precursor 2 (c) and precursor 3 (d)

Looking at figure (a) in Figure 44, the wear track of the specimen can be seen without precursor. It is significantly wider than the other 3 in Figures (b), (c) and (d). This is also in line with the measured COFs in Figure 42 (graph middle below) and the determined wear

rates in Figure 43. It is difficult to see a difference between precursor 1 (b) and precursor 2 (c). However, the COFs and wear rates in the previous figures do not differ as fundamentally as for the specimen without precursor. The wear track of precursor 3 (d) is noticeable. It is basically much narrower, but also differs topographically. It almost seems as if the steel surface was polished during the test.

4.5.4 XPS analysis

The following figure shows the XPS spectra of the samples at RT.

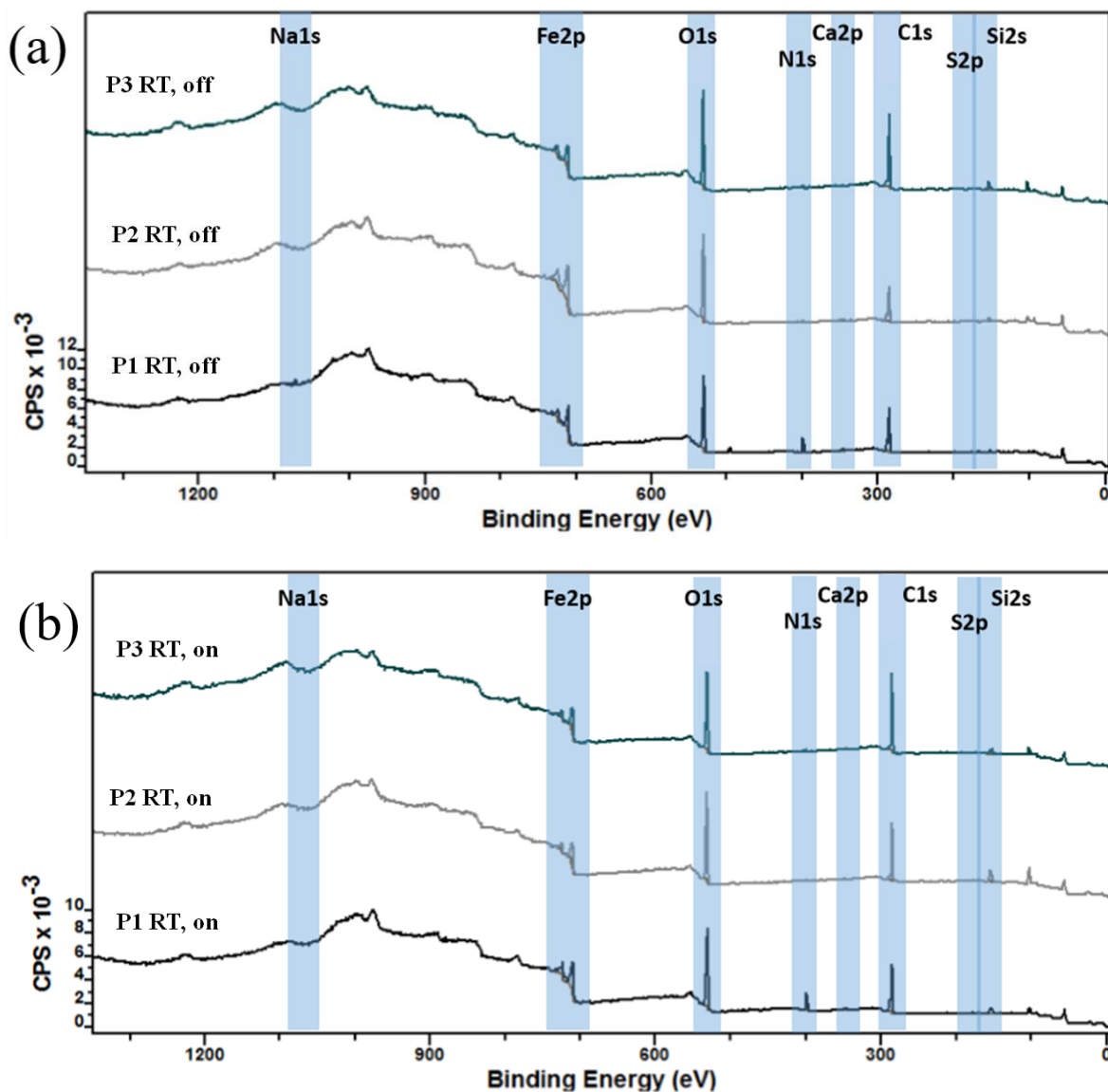


Figure 45: XPS survey spectra of all samples at RT off (a) and on (b) the wear tracks. The regions used for quantification are shown in blue. All spectra have been normalized to their strongest signals.

On all samples the elements C, Fe, O, N and Si can be found at all measuring positions. In addition, small amounts of Ca were detected in the samples, probably residues of distilled water used for sample cleaning. Traces of Na were found on the unaltered surface of samples 1 and 2, while Na could not be found on any of the wear tracks. In addition, small amounts of S were found on sample 1 and on the unaltered surface of sample 2. Traces of Cr were also found on some of the unaltered surfaces. However, this could be expected from the composition of the steel surface.

The relative amounts of O are lower on all wear tracks than on the unaltered surfaces. The amounts of C, Fe, Si and N also vary between untreated sample portions and wear tracks, with no clear trend visible on any of the samples.

Detail spectra analysis

Fe 2p detail spectra consist mainly of iron oxide (approximately 711 eV, probably Fe_2O_3). In addition, small amounts of Fe (706.6 eV) were found at all measuring points. A slight decrease of Fe was observed on the wear tracks, which may be due to an increase in iron oxide layer thickness.

The C1s narrow scan signal can be deconvoluted into three different components: C-C/C-H/Si- CH_3 at 284.8 eV, C-O/C-N at 286.3 eV and O-C=O/N=C=N around 288.5 eV.

For the O 1s signal, metal oxides are detected around 529.9 eV BE, Oxygen in organic compounds and in Si-O bonds are found around 531.8 eV. For sample 3 an increase in metal oxides is found on the wear tracks while a decrease in metal-oxides is detected for all other samples.

N1s detail spectra exhibit three different components: N-C/N organics around 400.0 eV, (Si-)N=C/N organics at 398.7 eV and Si-N at 397.2 eV [70, 71]. It has to be noted that a distinction of other organic compounds from the precursor is complicated. However, as the bis(trimethylsilyl)carbodiimide only exhibits one bonding environment for N, it is assumed that the precursor partly decomposed on sample 1 on both measurement spots. While the origin of the N1s signal on samples 2 and 3 remains unclear, it has to be noted that it is found at a similar BE as the Si-N=C / N organics signal from sample 1.

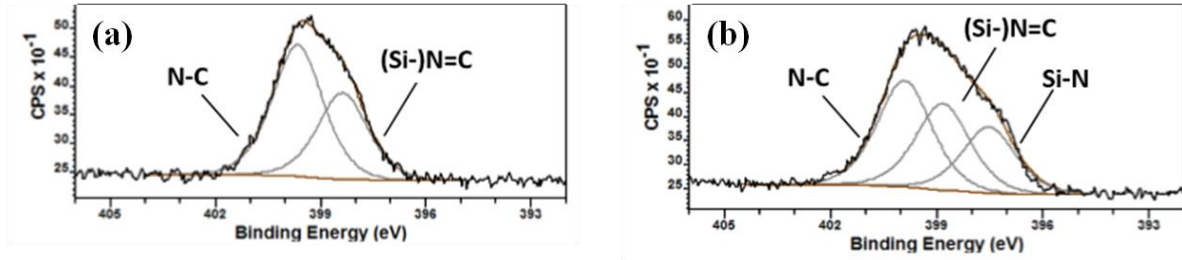


Figure 46: N 1s XPS detail spectra of sample 1 at RT (a) off and (b) on the wear tracks. All spectra have been normalised to their strongest signals.

Figure 46 shows an example of a deconvolution of the N 1s signal for precursor 1 at RT.

Finally, the Si 2p signal was deconvoluted into three signals for sample 1: SiOx signals were found around 103.0 eV, Si-N=C/Siloxane at 102.1 eV [72] and Si-Si at 99.8 eV BE. The assumption has been made that no (SiC-containing) ceramics are formed in the wear tracks but the precursors still decompose as Si-Si bonds have been found on all samples. However, while the Si-N=C/Siloxane component is decreased no increase in Si-Si content has been detected in most of the wear tracks.

The XPS spectra of the samples at 100 °C are depicted in Figure 47.

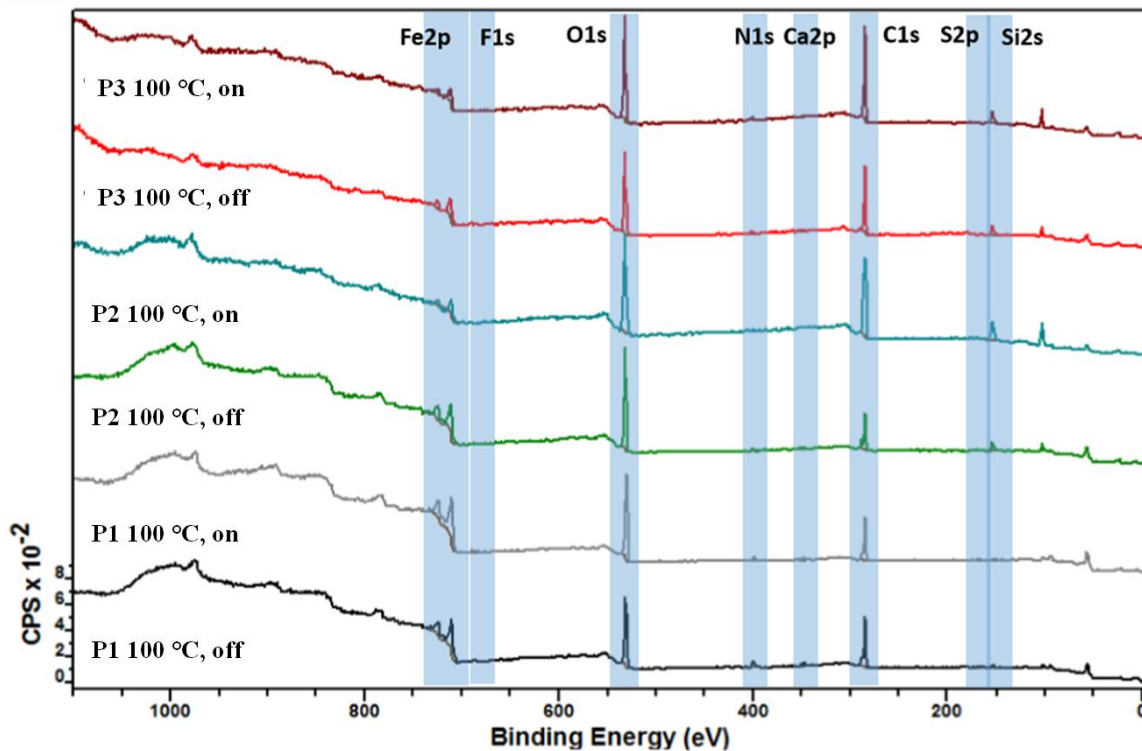


Figure 47: XPS survey spectra of all samples at 100 °C on and off the wear tracks. The regions used for quantification are shown in. All spectra have been normalised to their strongest signals.

Again at 100 °C all samples show the elements C, Fe, O, Si and N at all measuring positions. Also all samples showed small amounts of Ca. As discussed above, this is probably

related to the cleaning process. F and S were only found on sample 1. Traces of Cr contained in the steel were also found on most samples.

Samples 2 and 3 showed increases in C and Si content and decreases in Fe, O and N content on the wear tracks, while samples of precursor 1 showed decreases in C, N and Si content and increases in Fe and O content.

Detail spectra analysis

The results of the detail spectra analysis are quite similar to the samples treated at RT.

A slight decrease of Fe was observed on the wear tracks, which may be due to an increase in iron oxide layer thickness.

The most notable change in C composition is found on the wear track of sample 2 where the C-O content is significantly increased in comparison to the unaltered steel surface. Similarly, an increase in C-O content is observed in O1s spectra.

The spectra of the samples treated at 80 °C for 30 minutes are shown in Figure 48.

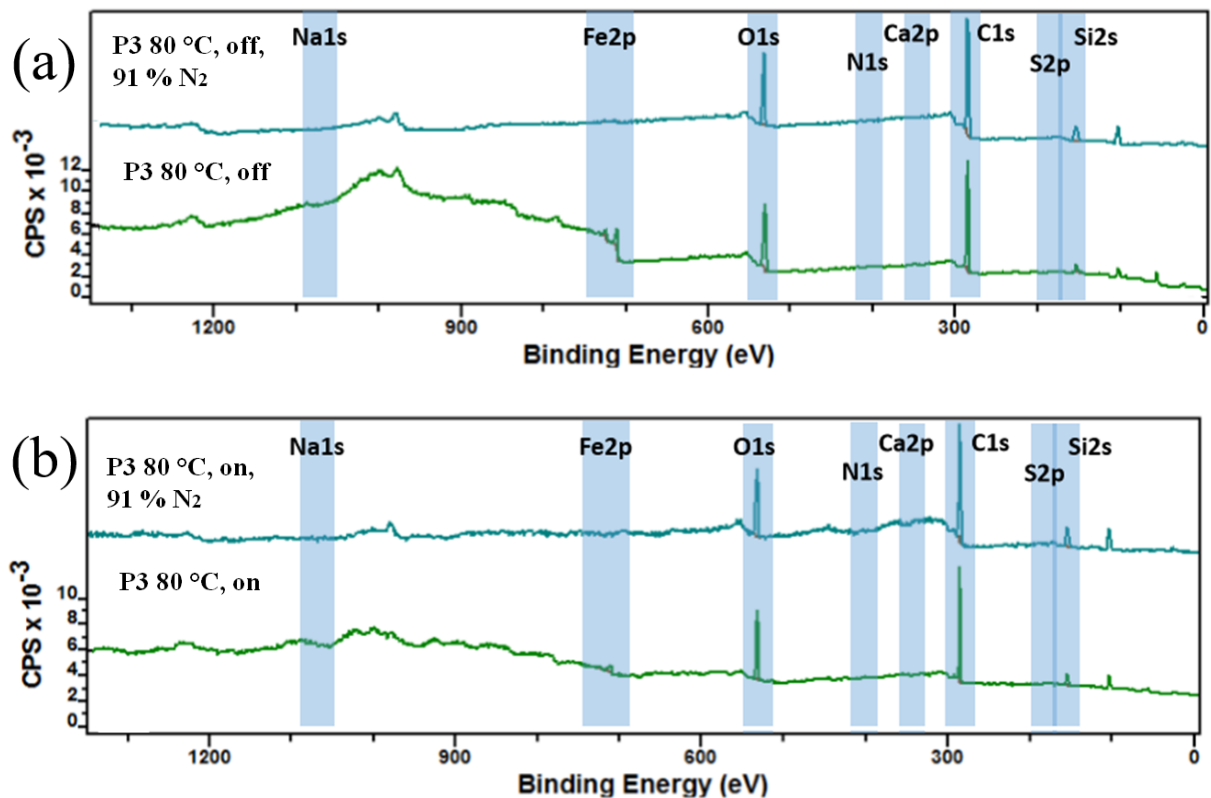


Figure 48: XPS survey spectra of the samples at 80 °C off (a) and on (b) the wear tracks. The regions used for quantification are shown in. All spectra have been normalized to their strongest signals.

In contrast to all other samples (Figure 45 and Figure 47), no N could be detected on these samples.

The detail spectra of precursor 3 under 91 % N₂ atmosphere could not be analyzed because a thicker layer of Si/C material probably caused charging effects and thus shifted and broadened the peaks.

In contrast to the previous measurements, no N 1s signal could be found on the sample, which was treated at 80 °C for 30 min. Also the C=O component in the C 1s signal could not be found on the wear track of this sample.

5 Conclusion

The following conclusions can be drawn on the basis of the results obtained:

- While for precursor 1 and 2 the friction increased significantly with increasing temperature, for precursor 3 this effect was much lower or in some cases even opposite. A similar effect has already been observed with the polymer of precursor 3 [5]. Consequently, the wear and the visible track of precursor 3 are also considerably smaller than that of the other samples. These results make trimethoxyphenylsilane the most promising of the 3 precursors for possible use in hot forming processes.
- Tribofilms have been successfully formed. Due to their low thickness, however, it was not possible to determine their structure (amorphous/crystalline) by electron diffraction. Also the chemical composition could only be determined partially.
- No ceramic-like (SiC) tribological layers could be detected with certainty. However, all precursors might decompose in some way, since Si-Si bonds could be detected on all samples.
- In accordance with former research time [73] and atmosphere [74] are likely to have a considerable influence on the friction behaviour and tribofilm formation, as no XPS measurements could be carried out in the friction tests under elevated nitrogen atmosphere when the test duration was extended to 30 min due to a thicker Si/C-containing layer and the associated charging effects. This sample could also have a tribofilm thick enough to apply electron diffraction in order to determine the structure.

6 Outlook

There are some interesting approaches for future research regarding this topic:

- Since the generated tribolayers are only a few nanometers thin (as can be seen in TEM images), it would be interesting to consider an additional surface-specific analysis method, such as AES.
- The testing of further precursors would also be interesting. For example, there are other organosilicon compounds with higher boiling points [75]. It would also be conceivable to carry out experiments with the polymerised variants of precursor 1 and 3.
- The combination of a selected precursor with ZDDP as additive and its effect on wear would be another possibility to continue this research topic.

Nomenclature

AE	Auger electrons
AES	Auger electron spectroscopy
BF	bright-field
BSE	Backscattered electron
BTSC	Bis(trimethylsilyl)carbodiimide
COF	Coefficient of friction
CCD	Charge-coupled device
CL	Cathodoluminescence
DCM	Differential confocal microscope
DF	dark-field
E_B	Binding energy
EDX	Energy dispersive X-ray spectroscopy
FIB	Focused ion beam
IL	Ionic liquid
N_B	Number of beam electrons
N_{BSE}	Number of emerging backscattered electrons
N_{SE}	Number of secondary electrons emitted from the sample
PDC	Polymer derived ceramic
RT	Room temperature
SE	Secondary electron
SEM	Scanning electron microscope
SRV	Schwing-Reib-Verschleiß Tribometer
TEM	Transmission electron microscope

XPS X-ray photoelectron spectroscopy

ZDDP Zinc dialkyldithiophosphate

δ N_{SE}/N_B

λ liquid film-thickness/roughness

μ Coefficient of friction

μ kinematic viscosity

f Coefficient of friction

η backscattered electron coefficient

η dynamic viscosity

ρ density

h Planck constant

k wear rate

References

1. Holmberg, K., Andersson, P., & Erdemir, A. (2012). Global energy consumption due to friction in passenger cars. *Tribology International*, *47*, 221–234. doi:10.1016/j.triboint.2011.11.022
2. Fischer, T. E. (1992). Chemical Effects in Friction. In I. L. Singer & H. M. Pollock (Eds.), *Fundamentals of Friction: Macroscopic and Microscopic Processes* (pp. 299–312). Dordrecht: Springer Netherlands. doi:10.1007/978-94-011-2811-7_16
3. Wen, S., & Huang, P. (2018). *Principles of tribology* (Second edition.). Hoboken, NJ: Wiley.
4. Gosvami, N. N., Bares, J. A., Mangolini, F., Konicek, A. R., Yablon, D. G., & Carpick, R. W. (2015). Mechanisms of antiwear tribofilm growth revealed in situ by single-asperity sliding contacts. *Science*, *348*(6230), 102–106. doi:10.1126/science.1258788
5. Gonzalez Rodriguez, P., Dral, A., van den Nieuwenhuijzen, K., Lette, W., Schipper, D., & ten Elshof, J. (2018). Thermochemical Stability and Friction Properties of Soft Organosilica Networks for Solid Lubrication. *Materials*, *11*(2), 180. doi:10.3390/ma11020180
6. Colombo, P., Mera, G., Riedel, R., & Sorarù, G. D. (2010). Polymer-Derived Ceramics: 40 Years of Research and Innovation in Advanced Ceramics: Polymer-Derived Ceramics. *Journal of the American Ceramic Society*, no-no. doi:10.1111/j.1551-2916.2010.03876.x
7. Mang, T., Bobzin, K., & Bartels, T. (2010). *Industrial Tribology: Tribosystems, Friction, Wear and Surface Engineering, Lubrication*. Weinheim, Germany: Wiley-VCH Verlag GmbH & Co. KGaA. doi:10.1002/9783527632572
8. Amontons, Guillaume. (1699). De la Resistance Causée dans les Machines. *Histoire Acad. Roy. Sci. Paris*, (12), 206.
9. Czichos, H., & Habig, K.-H. (Eds.). (2015). *Tribologie-Handbuch: Tribometrie, Tribomaterialien, Tribotechnik* (4., vollst. überarb. und erw. Aufl.). Wiesbaden: Springer Vieweg.
10. Woydt, M., & Wäsche, R. (2010). The history of the Stribeck curve and ball bearing steels: The role of Adolf Martens. *Wear*, *268*(11–12), 1542–1546. doi:10.1016/j.wear.2010.02.015
11. Deters, L. (2018). Reibung, Verschleiß und Schmierung. In B. Sauer (Ed.), *Konstruktionselemente des Maschinenbaus 2: Grundlagen von Maschinenelementen für Antriebsaufgaben* (pp. 1–68). Berlin, Heidelberg: Springer Berlin Heidelberg. doi:10.1007/978-3-642-39503-1_1

12. Stribeck, Richard. (1901). Kugellager für beliebige Belastungen. *Zeitschrift des Vereins Deutscher Ingenieure*, 45(3), 73–79.
13. Stribeck, Richard. (1902). Die wesentlichen Eigenschaften der Gleit- und Rollenlager. *Zeitschrift des Vereins Deutscher Ingenieure*, 46(36), 1341–1348, 1432–1438, 1463–1470.
14. Halling, J. (1975). A contribution to the theory of mechanical wear. *Wear*, 34(3), 239–249. doi:10.1016/0043-1648(75)90093-9
15. Quinn, T. F. J. (1962). Role of oxidation in the mild wear of steel. *British Journal of Applied Physics*, 13(1), 33–37. doi:10.1088/0508-3443/13/1/308
16. Archard, J. F. (1953). Contact and Rubbing of Flat Surfaces. *Journal of Applied Physics*, 24(8), 981–988. doi:10.1063/1.1721448
17. Kajdas, C. K. (2005). Importance of the triboemission process for tribochemical reaction. *Tribology International*, 38(3), 337–353. doi:10.1016/j.triboint.2004.08.017
18. Rosenkranz, A., Reinert, L., Gachot, C., & Mücklich, F. (2014). Alignment and wear debris effects between laser-patterned steel surfaces under dry sliding conditions. *Wear*, 318(1–2), 49–61. doi:10.1016/j.wear.2014.06.016
19. Gachot, C., Rosenkranz, A., Reinert, L., Ramos-Moore, E., Souza, N., Müser, M. H., & Mücklich, F. (2013). Dry Friction Between Laser-Patterned Surfaces: Role of Alignment, Structural Wavelength and Surface Chemistry. *Tribology Letters*, 49(1), 193–202. doi:10.1007/s11249-012-0057-y
20. Reinert, L., Lasserre, F., Gachot, C., Grützmacher, P., MacLucas, T., Souza, N., ... Suarez, S. (2017). Long-lasting solid lubrication by CNT-coated patterned surfaces. *Scientific Reports*, 7(1). doi:10.1038/srep42873
21. DIN 8580:1974-06. (n.d.). *Fertigungsverfahren - Begriffe, Einteilung*.
22. Kuchling, H. (1985). *Taschenbuch der Physik* (5.-7. Aufl.). Thun: Deutsch.
23. Nyberg, E., Mouzon, J., Grahn, M., & Minami, I. (2017). Formation of Boundary Film from Ionic Liquids Enhanced by Additives. *Applied Sciences*, 7(5), 433. doi:10.3390/app7050433
24. Kapsa, P., & Martin, J. M. (1982). Boundary lubricant films: a review. *Tribology International*, 15(1), 37–42. doi:10.1016/0301-679X(82)90110-4
25. Hsu, S. M., & Gates, R. S. (2005). Boundary lubricating films: formation and lubrication mechanism. *Tribology International*, 38(3), 305–312. doi:10.1016/j.triboint.2004.08.021

26. Qu, J., Chi, M., Meyer, H. M., Blau, P. J., Dai, S., & Luo, H. (2011). Nanostructure and Composition of Tribo-Boundary Films Formed in Ionic Liquid Lubrication. *Tribology Letters*, *43*(2), 205–211. doi:10.1007/s11249-011-9800-z
27. Morina, A., & Neville, A. (2007). Tribofilms: aspects of formation, stability and removal. *Journal of Physics D: Applied Physics*, *40*(18), 5476–5487. doi:10.1088/0022-3727/40/18/S08
28. BOWDEN, F. P., GREGORY, J. N., & TABOR, D. (1945). Lubrication of Metal Surfaces by Fatty Acids. *Nature*, *156*, 97.
29. Biswas, S. . (2000). Some mechanisms of tribofilm formation in metal/metal and ceramic/metal sliding interactions. *Wear*, *245*(1–2), 178–189. doi:10.1016/S0043-1648(00)00477-4
30. Spikes, H. (2004). The History and Mechanisms of ZDDP. *Tribology Letters*, *17*(3), 469–489. doi:10.1023/B:TRIL.0000044495.26882.b5
31. Barnes, A. M., Bartle, K. D., & Thibon, V. R. A. (2001). A review of zinc dialkyldithiophosphates (ZDDPS): characterisation and role in the lubricating oil. *Tribology International*, *34*(6), 389–395. doi:10.1016/S0301-679X(01)00028-7
32. Zhang, J., & Spikes, H. (2016). On the Mechanism of ZDDP Antiwear Film Formation. *Tribology Letters*, *63*(2). doi:10.1007/s11249-016-0706-7
33. Fuller, M. L. S., Kasrai, M., Bancroft, G. M., Fyfe, K., & Tan, K. H. (1998). Solution decomposition of zinc dialkyl dithiophosphate and its effect on antiwear and thermal film formation studied by X-ray absorption spectroscopy. *Tribology International*, *31*(10), 627–644. doi:10.1016/S0301-679X(98)00084-X
34. Martin, J. M., Onodera, T., Minfray, C., Dassenoy, F., & Miyamoto, A. (2012). The origin of anti-wear chemistry of ZDDP. *Faraday Discussions*, *156*, 311. doi:10.1039/c2fd00126h
35. Matic, A., & Scrosati, B. (2013). Ionic liquids for energy applications. *MRS Bulletin*, *38*(07), 533–537. doi:10.1557/mrs.2013.154
36. Ye, C., Liu, W., Chen, Y., & Yu, L. (n.d.). Room-temperature ionic liquids: a novel versatile lubricant, 2.
37. Landauer, A. K., Barnhill, W. C., & Qu, J. (2016). Correlating mechanical properties and anti-wear performance of tribofilms formed by ionic liquids, ZDDP and their combinations. *Wear*, *354–355*, 78–82. doi:10.1016/j.wear.2016.03.003

38. Pump, J., & Wannagat, U. (1962). Beiträge zur Chemie der Silicium-Stickstoff-Verbindungen, XIV. Bis-trimethylsilyl-carbodiimid. *Justus Liebigs Annalen der Chemie*, 652(1), 21–27. doi:10.1002/jlac.19626520104
39. Sigma-Aldrich. (2017). Safety Data Sheet of Bis(trimethylsilyl)carbodiimide according to Regulation (EC) No. 1907/2006. Retrieved from <https://www.sigmaaldrich.com/MSDS/MSDS/DisplayMSDSPage.do?country=AT&language=EN-generic&productNumber=344338&brand=ALDRICH&PageToGoToURL=https%3A%2F%2Fwww.sigmaaldrich.com%2Fcatalog%2Fproduct%2Faldrich%2F344338%3Flang%3Dde>
40. Zhou, Y., Probst, D., Thissen, A., Kroke, E., Riedel, R., Hauser, R., ... Stafast, H. (2006). Hard silicon carbonitride films obtained by RF-plasma-enhanced chemical vapour deposition using the single-source precursor bis(trimethylsilyl)carbodiimide. *Journal of the European Ceramic Society*, 26(8), 1325–1335. doi:10.1016/j.jeurceramsoc.2005.02.004
41. Sigma-Aldrich. (2018). Safety Data Sheet of Poly(methylphenylsiloxane) according to Regulation (EC) No. 1907/2006. Retrieved from <https://www.sigmaaldrich.com/MSDS/MSDS/DisplayMSDSPage.do?country=AT&language=EN-generic&productNumber=378496&brand=ALDRICH&PageToGoToURL=https%3A%2F%2Fwww.sigmaaldrich.com%2Fcatalog%2Fproduct%2Faldrich%2F378496%3Flang%3Dde>
42. Sigma-Aldrich. (2016). Safety Data Sheet of Trimethoxyphenylsilane according to Regulation (EC) No. 1907/2006. Retrieved from <https://www.sigmaaldrich.com/MSDS/MSDS/DisplayMSDSPage.do?country=AT&language=EN-generic&productNumber=435651&brand=ALDRICH&PageToGoToURL=https%3A%2F%2Fwww.sigmaaldrich.com%2Fcatalog%2Fproduct%2Faldrich%2F435651%3Flang%3Dde>
43. Shu, D., & Zhang, D. (2015). SELF-ASSEMBLY OF TMTES–GO–APS ON Si SUBSTRATE AND THE TRIBOLOGICAL PROPERTIES OF THE MULTILAYER FILM. *Surface Review and Letters*, 22(02), 1550023. doi:10.1142/S0218625X15500237
44. DIN 51834-1:2010-11. (n.d.). Prüfung von Schmierstoffen – Tribologische Prüfung im translatorischen Oszillations-Prüfgerät – Teil 1: Allgemeine Arbeitsgrundlagen.

45. Naredi-Rainer, N., Prescher, J., Hartschuh, A., & Lamb, D. C. (2013). Confocal Microscopy. In U. Kubitschek (Ed.), *Fluorescence Microscopy* (pp. 175–213). Weinheim, Germany: Wiley-VCH Verlag GmbH & Co. KGaA. doi:10.1002/9783527671595.ch5
46. Goldstein, J. (2017). *Scanning electron microscopy and x-ray microanalysis* (4th edition.). New York, NY: Springer Science+Business Media, LLC.
47. Wang, R., Wang, C., Zhang, H., Tao, J., & Bai, X. (Eds.). (2018). *Progress in nanoscale characterization and manipulation*. Beijing: Peking University Press.
48. Wikipedia. (n.d.). Electron Microscope. Retrieved 6 March 2019, from https://en.wikipedia.org/wiki/Electron_microscope
49. Gottschalk, M. (n.d.). Anwendungen der Ionen- & Elektronenmikroskopie im Grenzgebiet zwischen Nanostrukturphysik und Biologie, 116.
50. Schrader, B. (Ed.). (1995). *Infrared and Raman Spectroscopy*. Weinheim, Germany: Wiley-VCH Verlag GmbH. doi:10.1002/9783527615438
51. Stokes, George Gabriel. (1852). XXX. On the change of refrangibility of light. *Philosophical Transactions of the Royal Society of London*, 142, 463–562. doi:10.1098/rstl.1852.0022
52. Vandenabeele, P. (2013). *Practical Raman Spectroscopy - An Introduction: Vandenabeele/Practical Raman Spectroscopy - An Introduction*. Chichester, UK: John Wiley & Sons, Ltd. doi:10.1002/9781119961284
53. McCreery, R. L. (2000). *Raman spectroscopy for chemical analysis*. New York: John Wiley & Sons.
54. Yao, N. (Ed.). (2007). *Focused Ion Beam Systems: Basics and Applications*. Cambridge: Cambridge University Press. doi:10.1017/CBO9780511600302
55. Giannuzzi, L. A., & Stevie, F. A. (Eds.). (2005). *Introduction to focused ion beams: instrumentation, theory, techniques, and practice*. New York: Springer.
56. Thomas, J. M., & Ducati, C. (2012). Transmission Electron Microscopy. In M. Che & J. C. Védrine (Eds.), *Characterization of Solid Materials and Heterogeneous Catalysts* (pp. 655–701). Weinheim, Germany: Wiley-VCH Verlag GmbH & Co. KGaA. doi:10.1002/9783527645329.ch16
57. Einstein, A. (1905). Über einen die Erzeugung und Verwandlung des Lichtes betreffenden heuristischen Gesichtspunkt. *Annalen der Physik*, 322(6), 132–148. doi:10.1002/andp.19053220607

58. Friedbacher, G., & Bubert, H. (Eds.). (2011). *Surface and Thin Film Analysis: A Compendium of Principles, Instrumentation, and Applications*. Weinheim, Germany: Wiley-VCH Verlag GmbH & Co. KGaA. doi:10.1002/9783527636921
59. Seah, M. P., & Dench, W. A. (1979). Quantitative electron spectroscopy of surfaces: A standard data base for electron inelastic mean free paths in solids. *Surface and Interface Analysis*, *1*(1), 2–11. doi:10.1002/sia.740010103
60. Chemie.de. (n.d.). Retrieved from <http://www.chemie.de/lexikon/Viskosit%C3%A4t.html> (accessed March 29, 2019).
61. AC2T research. (n.d.). Pool Lub-Geräte. Retrieved 6 March 2019, from <https://www.ac2t.at/en/competences/pools/lubricants-lubrication-lub/equipment-for-chemical-material-characterisation/>
62. DIN EN ISO 683-17. (n.d.). Für eine Wärmebehandlung bestimmte Stähle, legierte Stähle und Automatenstähle – Teil 17: Wälzlagerstähle (ISO 683-17:2014); Deutsche Fassung EN ISO 683-17:2014.
63. Bhattacharyya, A. S., & Mishra, S. K. (2010). Raman studies on nanocomposite silicon carbonitride thin film deposited by r.f. magnetron sputtering at different substrate temperatures. *Journal of Raman Spectroscopy*, *41*(10), 1234–1239. doi:10.1002/jrs.2588
64. Mera, G., Navrotsky, A., Sen, S., Kleebe, H.-J., & Riedel, R. (2013). Polymer-derived SiCN and SiOC ceramics – structure and energetics at the nanoscale. *Journal of Materials Chemistry A*, *1*(12), 3826. doi:10.1039/c2ta00727d
65. Kaspar, J., Graczyk-Zajac, M., & Riedel, R. (2013). Lithium insertion into carbon-rich SiOC ceramics: Influence of pyrolysis temperature on electrochemical properties. *Journal of Power Sources*, *244*, 450–455. doi:10.1016/j.jpowsour.2012.11.086
66. Peña-Alonso, R., Mariotto, G., Gervais, C., Babonneau, F., & Soraru, G. D. (2007). New Insights on the High-Temperature Nanostructure Evolution of SiOC and B-Doped SiBOC Polymer-Derived Glasses. *Chemistry of Materials*, *19*(23), 5694–5702. doi:10.1021/cm071203q
67. Oh, Sei J., Cook, D.C., & Townsend, H.E. (1998). Characterization of Iron Oxides Commonly Formed as Corrosion Products on Steel, *112*(1–4), 59–66.
68. Bio-Rad Laboratories, Inc. SpectraBase; SpectraBase Compound ID=b1s2ogUan2 SpectraBase Spectrum ID=ISkdK0gp3sp. (n.d.). Retrieved from <http://spectrabase.com/spectrum/ISkdK0gp3sp> (accessed Oct 18, 2018).

69. Bio-Rad Laboratories, Inc. SpectraBase; SpectraBase Compound ID=K0AFNGdD7kw SpectraBase Spectrum ID=AAGPoocGqPp. (n.d.). Retrieved from <http://spectrabase.com/spectrum/AAGPoocGqPp> (accessed Nov 16, 2018).
70. Yuan, W., Qu, L., Li, J., Deng, C., & Zhu, H. (2017). Characterization of crystalline SiCN formed during the nitridation of silicon and cornstarch powder compacts. *Journal of Alloys and Compounds*, 725, 326–333. doi:10.1016/j.jallcom.2017.07.170
71. Wu, M., Wen, Z., Jin, J., & Chowdari, B. V. R. (2016). Trimethylsilyl Chloride-Modified Li Anode for Enhanced Performance of Li–S Cells. *ACS Applied Materials & Interfaces*, 8(25), 16386–16395. doi:10.1021/acsami.6b02612
72. Zhao, J., Luo, W., Qi, L., Yuan, L., Huang, G., Huang, Y., & Weng, X. (2018). The High-Temperature Resistance Properties of Polysiloxane/Al Coatings with Low Infrared Emissivity. *Coatings*, 8(4), 125. doi:10.3390/coatings8040125
73. Shimizu, Y., & Spikes, H. A. (2016). The Tribofilm Formation of ZDDP Under Reciprocating Pure Sliding Conditions. *Tribology Letters*, 64(3), 46. doi:10.1007/s11249-016-0776-6
74. Sundberg, J., Nyberg, H., Särhammar, E., Nyberg, T., Jacobson, S., & Jansson, U. (2014). Influence of composition, structure and testing atmosphere on the tribological performance of W–S–N coatings. *Surface and Coatings Technology*, 258, 86–94. doi:10.1016/j.surfcoat.2014.09.061
75. Hsieh, F.-Y. (1997). Correlation of closed-cup flash points with normal boiling points for silicone and general organic compounds. *Fire and Materials*, 21(6), 277–282. doi:10.1002/(SICI)1099-1018(199711/12)21:6<277::AID-FAM617>3.0.CO;2-3

List of figures

Figure 1: Coefficient of friction adapted from [7]	2
Figure 2: Representation of a tribological system adapted from [7].....	3
Figure 3: <i>Stribeck</i> curve adapted from [10]	4
Figure 4: Detailed abrasion processes adapted from [7]	8
Figure 5: Reasons for tribochemical reaction	15
Figure 6: Structural formula of ZDDP [32]	16
Figure 7: Possible ceramic reaction products of organosilicon polymers after thermal decomposition adapted from [6].....	17
Figure 8: Structural formula of bis(trimethylsilyl)carbodiimide.....	17
Figure 9: Structural formula of poly(methylphenyl)siloxane	18
Figure 10: Structural formula of trimethoxyphenylsilane.....	18
Figure 11: Schematic of the Test Chamber adapted from [44].....	19
Figure 12: Electron beam interaction with the sample adapted from [48, 49].....	22
Figure 13: Possible scattering processes for light quanta adapted from [52].....	24
Figure 14: Curve showing the dependence of λ from the kinetic energy (eV), Compilation by <i>Seah</i> and <i>Dench</i> , adapted from [59]	27
Figure 15: Untreated SRV disc	29
Figure 16: SRV 5 tribometer located at the Austrian excellence center of tribology AC2T in Wiener Neustadt (left), and Optimol tribometer located at the technical university of Luleå (right).....	30
Figure 17: Coefficient of friction for no precursor at different temperatures	31
Figure 18: Wear rate for no precursor at different temperatures.....	32
Figure 19: SEM images of a wear track at 100 °C, (a) BSE image at the edge of the wear track, (b) SE image in the middle of the wear track.....	32
Figure 20: SEM image including the selected areas for the EDS analysis. Visible is the wear track of a sample at 100 °C	33
Figure 21: Coefficient of friction for precursor 1 at different temperatures (left) and the dependence of the kinematic viscosity on the temperature (right).....	34
Figure 22: Wear rate for precursor 1 at different temperatures.....	35
Figure 23: SEM images of a wear track, (a) BSE image of the track at RT at the edge, SE image of the track at RT, (c) BSE image of the track at the edge at 100 °C and (d) SE image of the track at 100 °C.....	36

Figure 24: SEM image including the selected areas for the EDS analysis. Visible is the wear track of a sample at RT (a) and at 100 °C (b)	36
Figure 25: Raman spectra for precursor 1 at RT at different positions in and off the wear track	37
Figure 26: Raman spectra for precursor 1 at 100 °C at different positions in and off the wear track.....	38
Figure 27: TEM image of a foil from the wear track of precursor 1 at 100 °C	39
Figure 28: Coefficient of friction of precursor 2 at different temperatures (left) and the dependence of the kinematic viscosity on the temperature (right).....	40
Figure 29: Wear rate for precursor 2 at different temperatures.....	41
Figure 30: SEM images of a wear track, (a) BSE image in the middle of the track at 100 °C, (b) SE image in the middle of the track at 100 °C	41
Figure 31: SEM image including the selected areas for the EDS analysis. Visible is the edge of the wear track of a sample at 100 °C	42
Figure 32: Raman spectra for precursor 2 at RT at different positions in and off the wear track	43
Figure 33: Raman spectra for precursor 2 at 100 °C at different positions in and off the wear track.....	44
Figure 34: Coefficient of friction of precursor 3 at different temperatures (left), the dependence of the kinematic viscosity on the temperature (right) and coefficient of friction of precursor 3 at different temperatures measured at LTU (below)	45
Figure 35: COF of precursor 3 at 80 °C under air and elevated N ₂ atmosphere (left) and COF of precursor 3 at stepwise elevated temperatures (right).....	46
Figure 36: Wear rate for precursor 3 at different temperatures.....	47
Figure 37: SEM images of a wear track, (a) BSE image at the edge of the track at RT, (b) SE image at the edge of the track at RT, (c) BSE image in the middle of the track at 100 °C, (d) SE image in the middle of the track at 100 °C	48
Figure 38: SEM image including the selected areas for the EDS analysis. Visible is the wear track of a sample at RT (a) and at 100 °C (b)	49
Figure 39: Raman spectra for precursor 3 at RT at different positions in and off the wear track	49
Figure 40: Raman spectra for precursor 3 at 100 °C at different positions in and off the wear track.....	50
Figure 41: TEM image of a foil from the wear track of precursor 3 at 100 °C	51

Figure 42: COF of all precursors including Shell Helix Ultra SN 0W-20 and PAO 8 at RT (top left), COF of all precursors at 50 °C (top right) and COF of all precursors at 100 °C (middle below)	52
Figure 43: Wear rate for all precursors at different temperatures	53
Figure 44: SE images of the wear track at 100 °C for no precursor (a), precursor 1 (b), precursor 2 (c) and precursor 3 (d).....	54
Figure 45: XPS survey spectra of all samples at RT off (a) and on (b) the wear tracks. The regions used for quantification are shown in blue. All spectra have been normalized to their strongest signals.	55
Figure 46: N 1s XPS detail spectra of sample 1 at RT (a) off and (b) on the wear tracks. All spectra have been normalised to their strongest signals.....	57
Figure 47: XPS survey spectra of all samples at 100 °C on and off the wear tracks. The regions used for quantification are shown in. All spectra have been normalised to their strongest signals.	57
Figure 48: XPS survey spectra of the samples at 80 °C off (a) and on (b) the wear tracks. The regions used for quantification are shown in. All spectra have been normalized to their strongest signals.	58

List of tables

Table 1: Important physical data of precursor 1	17
Table 2: Important physical data of precursor 2	18
Table 3: Important physical data of precursor 3	18
Table 4: Parameters for Raman analysis	24
Table 5: Chemical composition of 100Cr6 steel in wt% [62].....	29
Table 6: Fixed parameters for test execution	29